Physics of Fluids

RESEARCH ARTICLE | OCTOBER 05 2023

Data-driven turbulence anisotropy in film and effusion cooling flows

Christopher D. Ellis ; Hao Xia

Physics of Fluids 35, 105114 (2023)
https://doi.org/10.1063/5.0166685

Physics of Fluids ARTICLE pubs.aip.org/aip/pof

Data-driven turbulence anisotropy in film and effusion cooling flows

Cite as: Phys. Fluids **35**, 105114 (2023); doi: 10.1063/5.0166685
Submitted: 6 July 2023 · Accepted: 8 September 2023 ·
Published Online: 5 October 2023

Christopher D. Ellis[a] and Hao Xia

AFFILIATIONS

National Centre for Combustion and Aerothermal Technology, Department of Aeronautical and Automotive Engineering, Loughborough University, Loughborough LE11 3GR, United Kingdom

[a]Author to whom correspondence should be addressed: c.d.ellis@lboro.ac.uk

ABSTRACT

Film and effusion cooling flows contain complex flow that classical Reynolds-averaged Navier–Stokes (RANS) models struggle to capture. A tensor-basis neural network is employed to provide an anisotropic model that can reproduce the Reynolds stress fields of large-eddy simulations (LES). High-quality LES datasets are used to train, validate, and test a neural network model. *A priori* results show the model can reproduce the Reynolds stress field on a cooling case not present in the model's training. The neural networks are employed directly into RANS solver, augmenting a k-ω shear stress transport (SST) model, with conditioning applied. The model provided improvements to Reynolds stress, velocity, and temperature fields in cases not used to train the model, including a multi-hole case that differs from the single-hole geometry used to train the case. Underpredictions of the turbulent kinetic energy field, modeled with the SST transport equation, were found to lead to underpredictions in the neural network produced Reynolds stresses. Correcting this with the LES, resolved turbulent kinetic energy provided further agreement. The method found significant improvements to the surface cooling results that advance the current state-of-the-art in RANS modeling of film and effusion cooling flows.

I. INTRODUCTION

Film and effusion cooling flows are characterized by a cooled jet issuing into a hot crossflow (Fig. 1). In gas turbines, film and effusion cooling techniques are used to protect combuster and turbine components from the hot gas flow. Accurately, modeling these flows is important for establishing component lifetimes and design of cooling systems that can permit higher gas temperatures or reductions to coolant massflow that can permit increases in engine efficiency. However, classic Reynolds-averaged Navier–Stokes (RANS) simulations struggle to provide accurate solutions to the complex flow where a high degree of anisotropy is present.[1] Data-driven models using machine learning techniques have attracted wider usage in the fluid dynamics community and promise a solution to the stagnating field of turbulence modeling.[2]

RANS simulations of film cooling flows have featured in an array of published literature. Hoda and Acharya[3] investigate various k-ε turbulence model formulations, including a direct numerical simulation (DNS) informed model, a k-ω model, and two non-linear models, the Mayong-Kasagi model and the Speziale model. Results showed the models struggled to capture the downstream velocity field, although the DNS informed model provided a recirculation in good agreement with the experimental datasets. Acharya *et al.*[4] observed overpredictions in coolant jet penetration and underpredictions in the lateral spreading rate of the coolant jet across two-equation turbulence models and a Lam–Bremhost Reynolds stress transport model (RSTM). Walters and Leylek[5,6] show that a k-ε model provides overpredictions to the centerline cooling effectiveness in lower blowing ratio (BR) cases, but trends are captured. At high blowing ratios, the jet lift-off characteristics are not observed in the cooling effectiveness distributions. This highlighted the lack of non-linear anisotropy and its affect on coolant lateral spread. Furthermore, work by Harrison and Bogard[7] showed that a realizable k-ε, standard k-ω, and a RSTM provided poor predictions of coolant lateral spread. The k-ω model provided accurate predictions of lateral-averaged cooling effectiveness but overpredicted the centerline effectiveness, while the realizable k-ε model obtained reasonable centerline results and poor laterally averaged results. Improvements to cooling effectiveness results have been established at lower blowing ratios by Azzi and Jubran[8] using an anisotropic near-wall model by Bergeles *et al.*[9] but at higher blowing ratios, results were unable to predict the trends associated with coolant jet lift-off

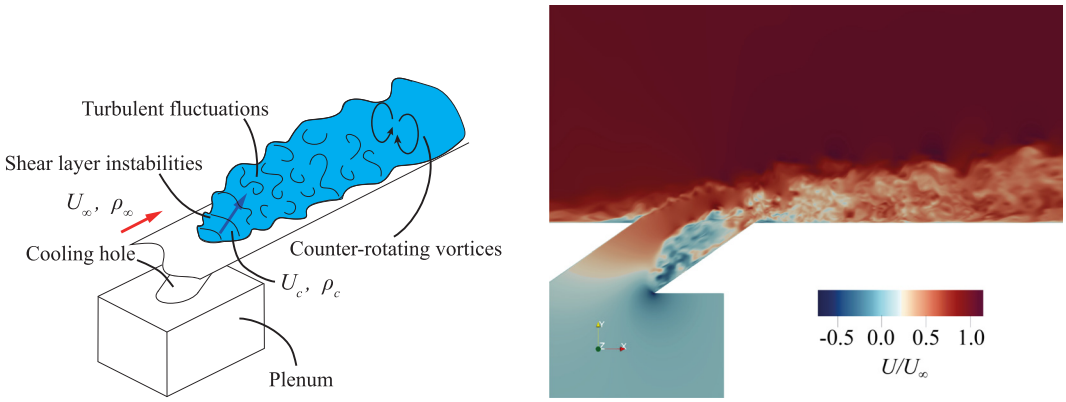

(a) Illustration (b) Instantaneous snapshot

FIG. 1. Film cooling flow and its physical features.

and reattachment. Large-eddy simulations (LES) have successfully replicated cooling effectiveness results in a range of numerical studies.[10–13] Ellis and Xia[14] demonstrated the LES predictions of coolant effectiveness are highly sensitive to the upstream flow and the turbulent fluctuations ahead of the coolant hole highlighting a need for a turbulent inflow boundary condition to match the experimental upstream conditions.

Data-driven modeling has recently become a constructive tool in the fluid mechanics community. Ling and Templeton[15] reviewed support vector machines, Adaboost decision trees, and random forest machine learning algorithms in their ability to assess model uncertainty of the Boussinesq hypothesis closure in RANS simulations. All three algorithms were successful in generalizing the error classifications to new flows not used in the training datasets. A tensor-basis neural network (TBNN) was established by Ling *et al.*[16] to model turbulent anisotropy and tested the framework on a simple small bump case where it predicted a separated region. Although the separation region was smaller than the observed DNS region, it improved upon linear and non-linear models where the separation was not observed. Marioni *et al.*[17] used a similar approach using shallow neural networks to provide simple, but effective, predictions of the tensor polynomial coefficients in the anisotropy. Gene Expression Programming (GEP) is a technique studied by Weatheritt and Sandberg[18,19] that has been used to establish a data-driven non-linear anisotropy term where the model was able to provide Reynolds stress predictions in a periodic hills case not used in the model training. Later work[19] was able to provide Reynolds stress predictions in duct and diffuser flow where the model was able to capture the secondary flow structures and showed improvements over linear and non-linear models.

In film cooling flows, Milani *et al.*[20] constructed a machine learnt turbulent diffusivity, for the gradient diffusion hypothesis (GDH) turbulent heat flux closure, trained on LES and DNS derived time-averaged turbulent diffusivity. Random forest algorithms were used and to train the model, and results showed a qualitative improvement in the Adiabatic Cooling Effectiveness (ACE) contours over the classic GDH closure with a constant turbulent Prandtl number. Later work by Milani *et al.*[21] investigated the use of the TBNN architecture of Ling *et al.*[16] for modeling a tensor-based turbulent diffusivity that permitted the turbulent heat flux to deviate from the GDH alignment to the temperature gradient. Results showed large improvements across the centerline plane but spanwise plane improvements were marginal. Ling *et al.*[22] investigated a random forest model approach that predicted barycentric coordinates associated with the turbulent anisotropy eigenvalues. Results showed good predictions of these coordinates and demonstrated generalization to a wavy wall and a square cylinder case but was not used in a RANS simulation to provide Reynolds stresses to the momentum equation. Ellis *et al.*[23] furthered the turbulent heat flux approach addressing the turbulent heat flux closure by formulating a machine learnt diffusivity coefficient for the higher-order generalized gradient diffusion hypothesis (HOGGDH). The model was constructed using random forest and shallow neural network algorithms providing accurate *a priori* results, but minor improvements were shown when the model was used in a full RANS simulation.

In this paper, we provide a method to model anisotropy using a well-studied neural network architecture applied to novel complex cases. High-fidelity LES simulations, that capture the flow physics, are generated to provide a database of accurate simulations validated against benchmark experiments. The neural network *a priori* results provide comparable anisotropy to LES data that the model was not trained on. A k-ω shear stress transport (SST) model is then augmented with the neural network model of anisotropy to provide realistic anisotropy in RANS models.

II. HIGH-FIDELITY LES DATASETS

A. Studied cases

LES is used to obtain well-resolved and accurate numerical results of single-row cylindrical cooling hole geometries at varying conditions. Five different cases are used in the training, validation, and testing datasets combining different single-row inclined cylindrical cooling hole geometries and different conditions. The five cases are summarized in Table I. The flow's blowing ratio and density ratio (DR) are established using Eqs. (1) and (2), respectively. The density and velocity parameters are illustrated in Fig. 1:

TABLE I. List of the studied cases, their respective conditions, and defining case names used throughout the report.

Case name	l/D	α	BR	DR	Re_j
s35-b05-d20	1.75	35°	0.5	2.0	15 125
s35-b10-d20	1.75	35°	1.0	2.0	30 250
l35-b10-d20	3.50	35°	1.0	2.0	30 250
m55-b04-d16	2.80	55°	0.4	1.6	10 770
m55-b10-d16	2.80	55°	1.0	1.6	10 770

$$BR = \frac{\rho_c U_c}{\rho_\infty U_\infty}, \tag{1}$$

$$DR = \frac{\rho_c}{\rho_\infty}. \tag{2}$$

Inclination angle and hole length define the coolant hole geometry. In the shorter holes, the separation bubble forming within the hole penetrates into mainstream flow, while a longer hole contains the separation to within the coolant hole. At large inclination angles, the flow has a larger normal velocity component and such cases promote jet lift-off, whereas shallower inclination angles provide a favorable environment for a fully attached cold jet. The inclination angle and hole length are defined in Table I. Additionally, these cooling cases feature a single row of cooling holes with a pitch separating the holes. For all the cases studied here, the experimental pitch is equal to 3*D*.

The five cases are experimentally investigated by Sinha *et al.*,[24] Pietrzyk *et al.*,[25,26] and Kohli and Bogard.[27] Experimental conditions are comparatively similar between the published cases. The experiments feature a continuously fed coolant plenum and a mainflow that runs across a plate featuring the cooling holes. The plate starts upstream of the cooling holes with a sharp leading edge initiating a fresh boundary layer that transitions prior to the coolant holes.

B. LES details

The LES data of case *s35-b10-d20* were presented in detail in the published work of Ellis and Xia[14] providing further detail on the LES strategy that has been used on the extended cases presented. Simulations have been performed using OpenFOAM v1712,[28] an open-source Computational Fluid Dynamics (CFD) suite that rivals common commercial packages that has attracted a wide range of users from the research community. It has developed traction in a broad range of fields such as jet flows,[29,30] combustion flows,[31] and two-phase flow,[32] among many others. The open-source, C++ class-based nature of OpenFOAM provides a suitable framework for research modifications and testing. A pressure-based solver suitable for transient flows, *rhoPimpleFoam*, is used in its Pressure Implicit Split Operator (PISO) mode, solving the filtered governing equations for continuity, momentum, and energy in the following forms, respectively:

$$\frac{\partial \bar{\rho}}{\partial t} + \frac{\partial \bar{\rho}\tilde{u}_i}{\partial x_i} = 0, \tag{3}$$

$$\frac{\partial \bar{\rho}\tilde{u}_i}{\partial t} + \frac{\partial \bar{\rho}\tilde{u}_i\tilde{u}_j}{\partial x_j} = -\frac{\partial \bar{p}}{\partial x_i} + \frac{\partial}{\partial x_j}\left(2\mu\tilde{S}^*_{ij} - \bar{\rho}\tau^{sgs}_{ij}\right), \tag{4}$$

$$\frac{\partial \bar{\rho}\tilde{h}_0}{\partial t} + \frac{\partial \bar{\rho}\tilde{u}_j\tilde{h}_0}{\partial x_j} = \frac{\partial}{\partial x_j}\left(\bar{\rho}\alpha\frac{\partial \tilde{h}}{\partial x_j} - \bar{\rho}q^{sgs}_j\right), \tag{5}$$

where

$$\tau^{sgs}_{ij} = -2\nu_{sgs}\tilde{S}^*_{ij} \tag{6}$$

and

$$\tilde{S}^*_{ij} = \frac{1}{2}\left(\frac{\partial \tilde{u}_i}{\partial x_j} + \frac{\partial \tilde{u}_j}{\partial x_i}\right) - \frac{1}{3}\frac{\partial \tilde{u}_k}{\partial x_k}. \tag{7}$$

Within the LES, the sub-grid scale stresses, τ^{sgs}_{ij}, are modeled using the wall-adaptive local eddy-viscosity (WALE) model.[33] The model provides correct near-wall scaling of the sub-grid-scale viscosity with y^3 without the requirement of a dynamic formulation. WALE has been successfully used within conjugate heat transfer simulations of cooled turbine blades,[34] the flow and heat transfer of two cylinders in tandem,[35] and rib-roughened internal turbine blade cooling channels.[36] The WALE model coefficient c_w is set to 0.325 that has become common practice in complex flows providing suitable diffusion.[37] The cube-root of the local cell volume is used as the filtered length scale. Sub-grid-scale heat fluxes are modeled with a sub-grid-scale Prandtl number, Pr_{sgs}, of 0.4. This value is used in LES simulations by Schindler *et al.*[38] and Eidson[39] and recommended by Grötzbach and Wörner.[40]

The computational domain is presented in Fig. 2 detailing the boundary conditions. Periodic boundaries are placed either side of the cooling hole a distance of $p/2$ from the coolant hole center to capture the spanwise pitch of the row of cooling holes featured in the experiment. The inflow boundary is placed 7*D* upstream of the cooling hole leading edge. The farfield boundary is placed 7*D* above the plate, as used by Chen,[41] permitting fluid to escape the domain and replicate the larger wind tunnel without the excessive computational cost.

At the mainstream inlet boundary, a digital filtering technique is used to capture the fluctuations of the approaching boundary layer featured in the experiment. Turbulent fluctuations upstream of the coolant hole are known to impact surface coolant distributions. Impact of freestream turbulence fluctuations has been documented by Mayhew *et al.*,[42] Kohli and Bogard,[43] and Ellis and Xia.[14] The near-wall turbulence of the upstream boundary layer has been shown to significantly impact the lateral coolant spread in the downstream jet. The use of an effective and representative turbulent inflow method is therefore critical in establishing accurate flow fields for use in data-driven models. The digital filtering technique is pursued in the current work, because of its ability to provide correlated turbulent fields in a simple manner. Inflow turbulence is generated at the inlet using a modification of the digital-filtered technique of Klein *et al.*[44] published by Immer[45] for use in urban flows. The boundary condition requires velocity, Reynolds stresses, and integral length scale profiles at the inlet to construct the turbulent inflow. The velocity and Reynolds stress profiles are taken from the experimental data of Pietrzyk *et al.*[25] The inflow boundary is placed 7*D* upstream of the coolant hole, allowing the synthetic turbulence to develop.

C. Meshing strategy

The meshing of the film cooling geometries is pursued using a well-organized hexahedral mesh, minimizing non-orthogonality and

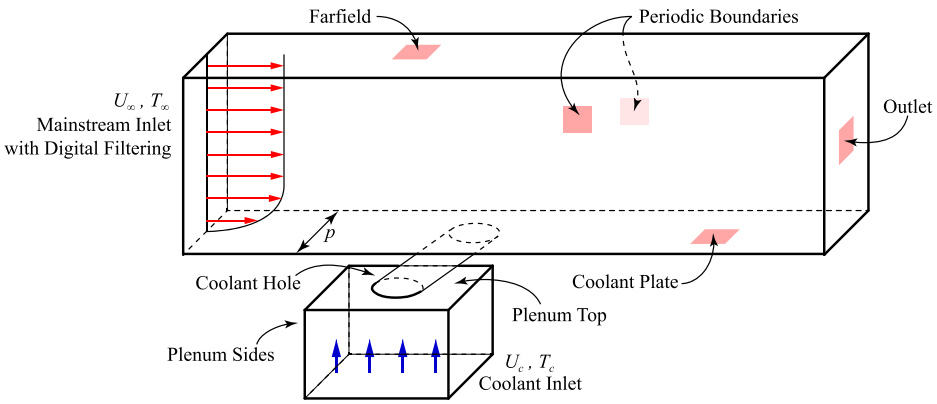

FIG. 2. Computational domain and defining boundary conditions.

skewness. This ensures numerical diffusivity, from the mesh, is minimal in regions, where mixing of the hot and cold gases is well featured. Figure 3 shows the meshing configuration for the medium-sized mesh applied in the present LES studies. The mesh around the coolant hole is achieved using an O-mesh configuration that surrounds the outside of the coolant hole allowing the circular geometry of the angled coolant hole to be resolved. A finer distribution of cells is provided around the cooling hole and immediately downstream of the coolant hole training edge where the flow is separated. Downstream of this region, the cell distribution in the streamwise direction is gradually coarsened.

Near the wall, cells are finely distributed to resolve the boundary layer flow. The wall adjacent cell has a normal height that achieves a maximum Δy^+ of unity, where $y^+ = yu_\tau/\nu$. In the streamwise and spanwise directions, cells are distributed to achieve high-quality LES resolution of the near-wall flow. Piomelli and Balaras[46] recommend cell sizes of $\Delta x^+ \simeq 100$ and $\Delta z^+ \simeq 20$, where x and z are the streamwise and spanwise coordinates, respectively, to resolve the inner-layer eddies of a turbulent boundary layer. Streamwise and spanwise cell sizes obtain a $\Delta x^+ < 26$ and $\Delta z^+ < 11$, respectively, in the upstream boundary layer flow. Aft of the hole trailing edge, a cell size of $\Delta x^+ < 23$ and $\Delta z^+ < 23$ is obtained. The resulting cell count of this medium-sized mesh for the s35 geometry is 20.6×10^6 cells.

The ratio of resolved to total turbulent kinetic energy, r_k, has been extracted from the simulation of case *l35-br10-dr20*. To show that the LES and its mesh are sufficient to resolve the large structures of the flow, it has become common practice to demonstrate that this ratio exceeds 80% across the domain. Pope[47] refers to a turbulence-resolution tolerance, ϵ_M, of 0.2 to adjust the gird in adaptive LES. This value of 0.2 corresponds to the resolution of 80% of the total turbulent kinetic energy commonly quoted in LES studies. Equation (8) shows the expression of this ratio, formulated from the resolved turbulent kinetic energy, k_{res}, and the sub-grid-scale turbulent kinetic energy, k_{sgs}, from the sub-grid-scale model used. Figure 4 shows contours of r_k at three streamwise slices through the coolant jet. At slice $X = -1.1D$, the smallest r_k value of 90% is present at the sides of the coolant hole, where the coolant and mainstream flow interact and vortices form at the coolant hole edge. Further downstream, the resolved turbulent kinetic energy makes a larger portion of the total turbulent kinetic energy

$$r_k = \frac{k_{res}}{k_{sgs} + k_{res}}. \tag{8}$$

D. Validation

To demonstrate the suitability of the LES, for constructing training, validation, and testing datasets, two simulations have been shown providing comparisons to experimental adiabatic cooling effectiveness,[24] velocity, and Reynolds stress profiles.[25,48] Figure 5 compares the adiabatic cooling effectiveness distributions for case *s35-br10-dr20* where jet lift-off and reattachment is observed and influences the surface cooling distribution. The LES results show comparable time-averaged data to the experimental work of Sinha *et al.*[24] The centerline distribution successfully captures the initial decrease in effectiveness followed by the secondary peak associated with the cooling jet reattachment. Likewise,

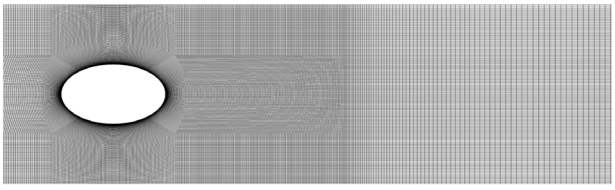

(a) Cooling plate surface mesh

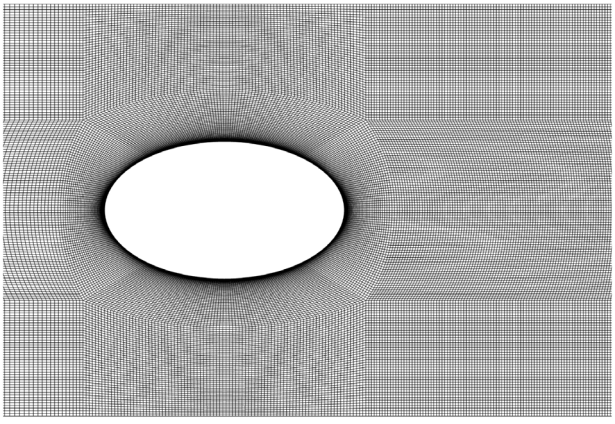

(b) Close-up view

FIG. 3. Mesh visualization across the plate surface showing fine hexahedral distributions in the regions of interest.

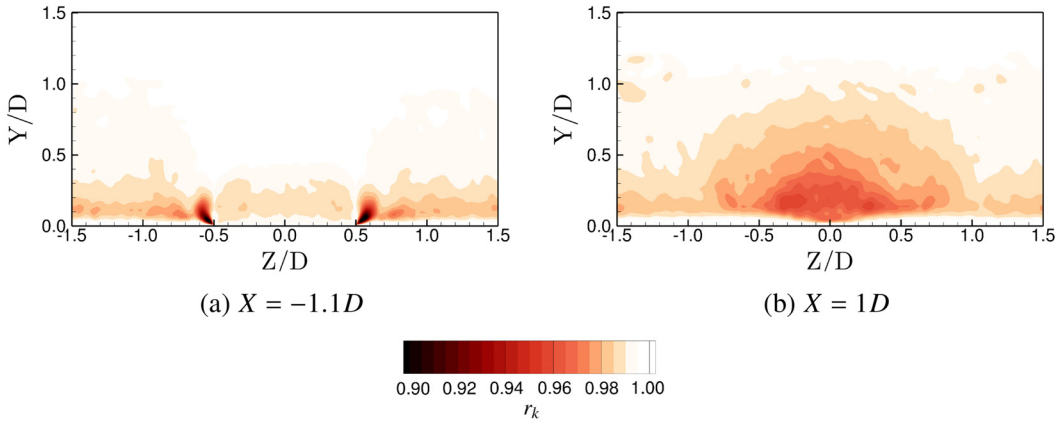

FIG. 4. Contours showing the ratio of resolved to total turbulent kinetic energy at three streamwise planes for *l35-br10-dr20*.

lateral cooling distributions show the LES simulation captures the correct lateral spreading behavior observed in the experiment.

Regarding the flow field, case *l35-br10-dr20* is compared to the experimental data of Pietrzyk *et al.*[25] (presented in further detail in Leedom[48]). Figure 6 shows the LES velocity profiles along the jet-centerline closely replicated those of the experiment, capturing the trends of the jet dynamics. The turbulent fluctuations, u_{rms}, v_{rms}, w_{rms}, and $\overline{u'v'}$ resolved by the LES, in Fig. 6, show the approach closely replicates the experimental measurements. Small differences are observed at $X = 3D$, a profile just downstream of the coolant hole trailing edge. Furthermore, downstream the profiles replicated the measurements of the LES and captured the trends in the turbulent behavior of the coolant jet.

The ability of the LES approach to accurately capture the experimental trends of cooling effectiveness, velocity, and turbulent fluctuations demonstrates its suitability for use in training, testing, and validating data-driven models. The mixing of the coolant jet and hot mainstream flow is accurately captured as evident by the downstream cooling predictions. The turbulent dynamics of the jet and the mean velocity profiles provides evidence that the LES Reynolds stresses and velocity fields are suitable for use in the datasets.

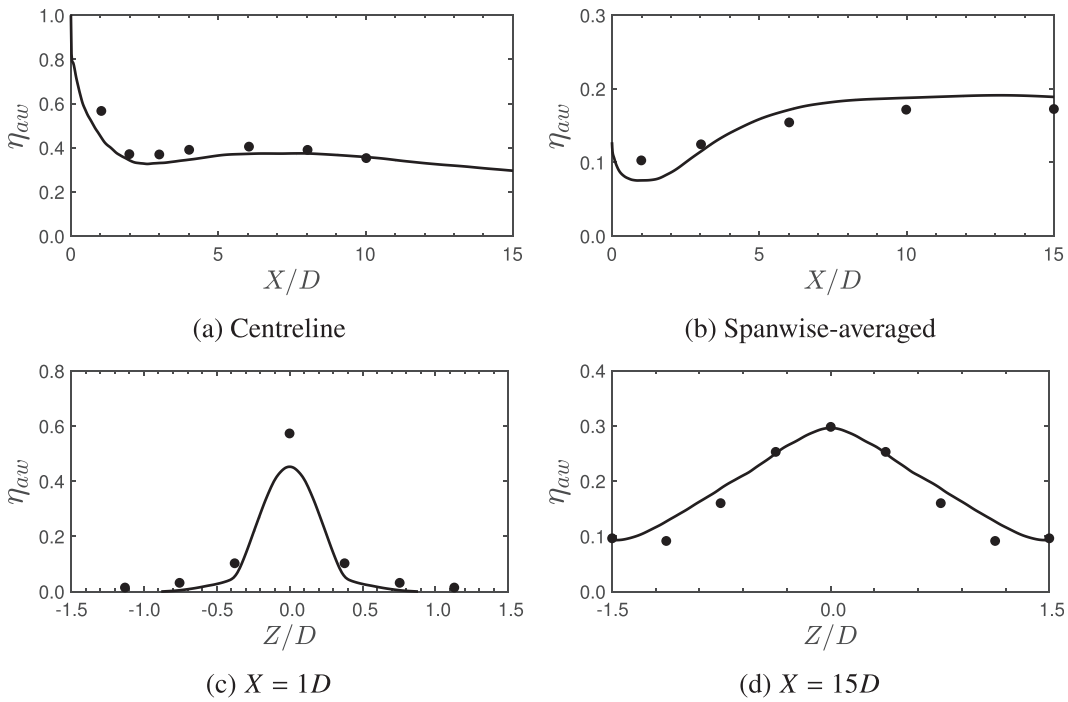

FIG. 5. Comparisons of LES surface ACE results (black line) for case *s35-br10-dr20* at $BR = 1.0$ and $DR = 2.0$ to experimental results of Sinha *et al.*[24] (black dot).

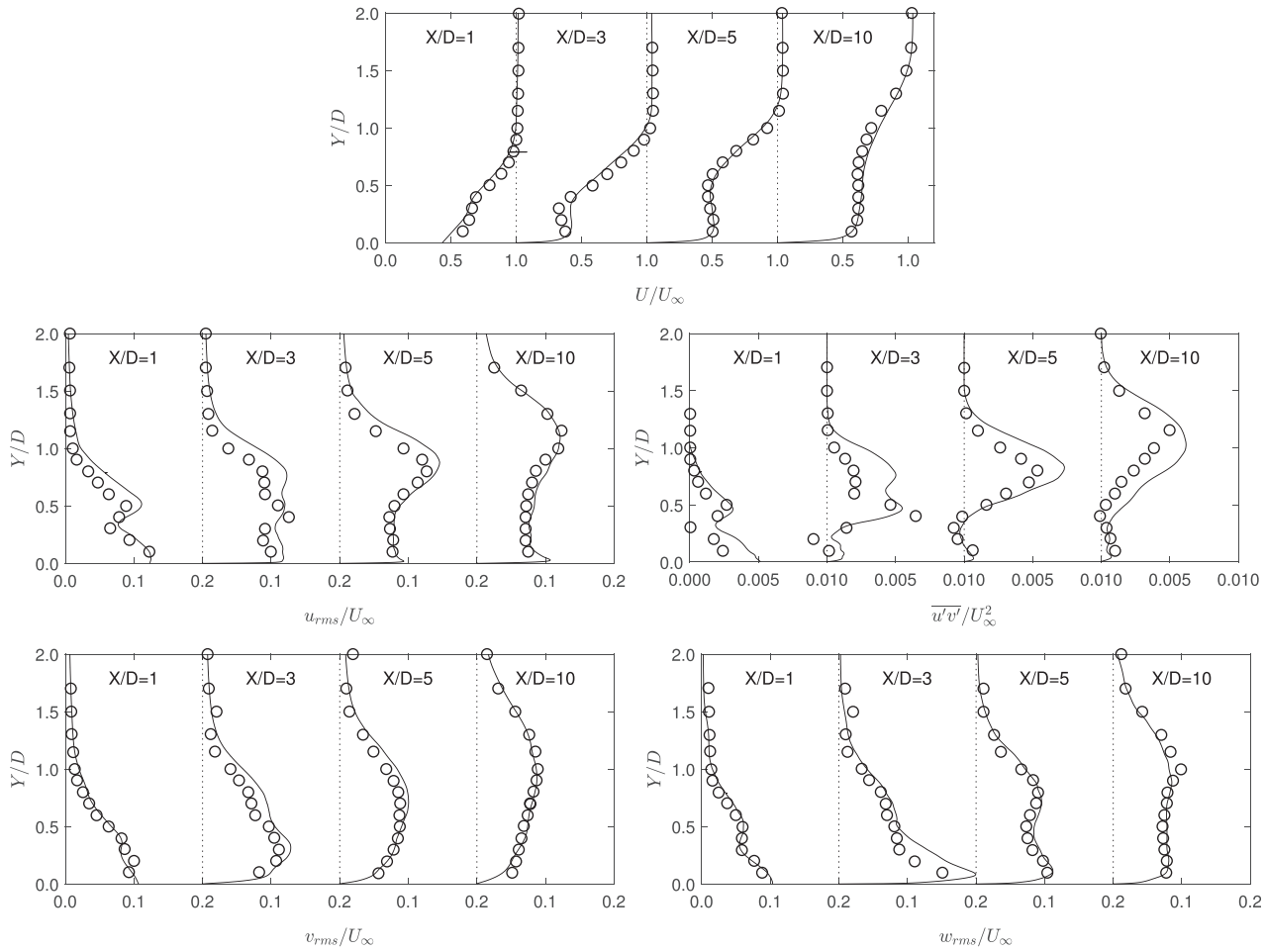

FIG. 6. Centerline profiles of key parameters resolved by the LES (black line) compared to experiment data (open circle) of Pietrzyk *et al.*[25] for *l35-br10-dr20*.

III. DATA-DRIVEN ANISOTROPY MODEL

A neural network approach is used to achieve a functional nonlinear model to provide accurate, highly anisotropic Reynolds stress fields. PyTorch,[49] an optimized tensor library for deep learning with central processing units (CPUs) and graphics processing units (GPUs), is used to produce the neural network models. The library allows for fast and flexible experimentation with neural networks, making it a strong candidate for research purposes. The PyTorch library also contains a sophisticated C++ application programming interface (API), enabling the models, investigated in Python, to be implemented in OpenFOAM's C++ code. The following is constructed using PyTorch 1.2.0.

The aim of the neural network methodology is to provide a function that will enable predictions of the Reynolds stress tensor, comparable to LES or experimental measurements, that classic two-equation turbulence models cannot provide. Instead of directly modeling the Reynolds stress tensor, the Reynolds stress anisotropy tensor is used as an intermediary variable. Anisotropy can then be used to determine the Reynolds stresses [Eq. (9)], with the turbulent kinetic energy, k, from the two-equation turbulence model. This approach is beneficial to neural networks because the anisotropy is non-dimensional and its components are well-bounded,

$$\overline{u_i' u_j'} = 2k\left(a_{ij} + \frac{1}{3}\delta_{ij}\right). \tag{9}$$

A. Network architecture

Pope[50] proposes a more general effective viscosity approach in which for a high Reynolds number, near-homogeneous flow, the Reynolds stresses are uniquely related to the strain rate, S_{ij}, the vorticity, W_{ij}, and two independent scaling parameters. The two independent scaling parameters, the turbulent kinetic energy, k, and the dissipation rate, ε, are combined to form the turbulent timescale, $\tau_t = k/\varepsilon$. This term is then used to scale and normalize the strain and vorticity rate tensors. A general expression for the anisotropy, a_{ij}, can then be made in the form of an infinite tensor polynomial, shown in the following equation:

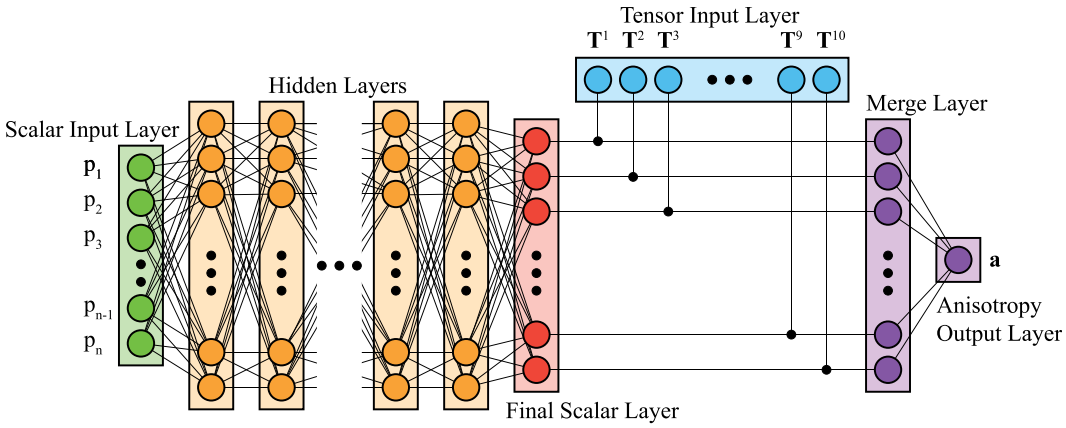

FIG. 7. Tensor-basis neural network (TBNN) architecture, published by Ling and Templeton[16] for Galilean invariant tensor regression.

$$a = \prod_{i=1}^{\infty} \sum_{\alpha_i=0}^{\infty} \prod_{j=1}^{\infty} \sum_{\beta_j=0}^{\infty} G^{\alpha_1,\alpha_2,\ldots}_{\beta_1,\beta_2,\ldots} s^{\alpha_1} w^{\beta_1} s^{\alpha_2} w^{\beta_2} \cdots. \tag{10}$$

Using the Cayley–Hamilton theorem, and acknowledging the traceless and symmetric nature of the anisotropy tensor, the infinite polynomial can be written as a finite polynomial with a finite number of invariants, shown by Eq. (11) and outlined by Pope.[50] Each tensorial term in the polynomial is traceless and symmetrical, ensuring that the anisotropy tensor is both traceless and symmetrical. For three-dimensional flows, there are 10 independent tensors and 5 independent invariants. Equation (11) captures the anisotropy using a sum of the products of tensors, $\boldsymbol{T}^i$, and their coefficients, λ_i. The coefficients are functions of the invariants and additional scalar inputs, p_n. For complex flows that deviate from the assumptions of Pope,[50] a set of additional scalar inputs have been sought,

$$a = \sum_{i=1}^{N} \lambda_i(p_1, p_2, \ldots, p_n) \boldsymbol{T}^i. \tag{11}$$

By considering the finite tensor polynomial of Eq. (11), a neural network architecture can be constructed that represents the function. The TBNN architecture (Fig. 7), recommended by Ling and Templeton,[16] differs from a standard input-hidden-output architecture by the addition of a merge layer, combining the output of the final scalar layer with a tensor input layer before the output layer. The terms in the final scalar layer form the coefficients, λ_i, shown in Eq. (11). The beginning of the network takes supplied inputs through a series of hidden layers with a number of hidden nodes prior to the final scalar layer. A preliminary hyperparameter study revealed that six hidden layers with 80 hidden neurons per layer provided the optimal validation error.

The final process within the output layer applies a limiter to the components of the output anisotropy to ensure the components are within realizable limits. The output bounds the normal, diagonal components of anisotropy between $-1/3$ and $2/3$, where $-1/3$ corresponds to a Reynolds stress value of zero and $2/3$ is for one-component turbulence where the Reynolds stress component is equal to $2k$ and the other normal components are zero. The off-diagonal, shear components are bound between $-1/2$ and $1/2$ set by the extreme limits of the Schwarz inequality $\overline{u_i'u_j'}^2 \leq \overline{u_i'u_i'u_j'u_j'}$.

B. Preprocessing datasets

The time-averaged high-fidelity LES data are interpolated onto a coarser, RANS appropriate mesh. This is achieved by coarsening the LES meshes in all spatial directions. Cell distributions are then adjusted to provide a near-wall cell size Δy^+ of 1. First, this provides a cell count that is 8 times smaller than the original LES grid, reducing the overall data and thus the time taken for model training. Second, the mesh downsampling smooths the LES time-averaged dataset without compromising on the quality of the data. Although the LES fields have been averaged for a significant time period, small amounts of noise can propagate to the gradients and other input parameters. By downsampling, the noise is reduced without compromising the quality of the LES fields.

Additionally, the datasets are reduced by only considering the data within the jet and near-wall flow. Outside of these regions, the Reynolds stress' impact on the momentum equation is close to negligible due to their small contribution in the transport equation. A blanking of the data, illustrated in Fig. 8, is performed before feeding the data to the neural network.

C. Input features

Input features for the TBNN model are highlighted in Tables II and III. The input features are split into two sets, tensor and scalar features, feeding their respective input layers. The tensor features come from the 10 independent traceless and symmetric tensor bases of the

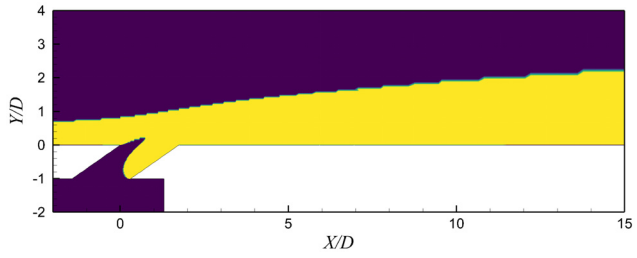

FIG. 8. Blanking ($k/U_\infty^2 > 0.0025$) used in the neural network training and validation datasets. Demonstrated on case *s35-br10-dr20*.

TABLE II. Independent invariants and tensors of the normalized strain-rate and rotational-rate tensors.

(a) Invariants

ID	Invariant
p1	$\{\boldsymbol{s}^2\}$
p2	$\{\boldsymbol{w}^2\}$
p3	$\{\boldsymbol{s}^3\}$
p4	$\{\boldsymbol{w}^2\boldsymbol{s}\}$
p5	$\{\boldsymbol{w}^2\boldsymbol{s}^2\}$

(b) Tensors

ID	Tensor
T1	$\boldsymbol{s}$
T2	$\boldsymbol{sw} - \boldsymbol{ws}$
T3	$\boldsymbol{s}^2 - \frac{1}{3}\boldsymbol{I}\{\boldsymbol{s}^2\}$
T4	$\boldsymbol{w}^2 - \frac{1}{3}\boldsymbol{I}\{\boldsymbol{w}^2\}$
T5	$\boldsymbol{ws}^2 - \boldsymbol{s}^2\boldsymbol{w}$
T6	$\boldsymbol{w}^2\boldsymbol{s} + \boldsymbol{sw}^2 - \frac{2}{3}\boldsymbol{I}\{\boldsymbol{sww}\}$
T7	$\boldsymbol{wsw}^2 - \boldsymbol{w}^2\boldsymbol{sw}$
T8	$\boldsymbol{sws}^2 - \boldsymbol{s}^2\boldsymbol{ws}$
T9	$\boldsymbol{w}^2\boldsymbol{s}^2 + \boldsymbol{s}^2\boldsymbol{w}^2 - \frac{2}{3}\boldsymbol{I}\{\boldsymbol{s}^2\boldsymbol{w}^2\}$
T10	$\boldsymbol{ws}^2\boldsymbol{w}^2 - \boldsymbol{w}^2\boldsymbol{s}^2\boldsymbol{w}$

normalized strain and vorticity rate, discussed by Pope[50] and shown in Table II(b). The first five scalar inputs are the invariants of the normalized strain and vorticity rate presented in Table II(a). The additional scalar features, used in works of Ling and Templeton[15] and Wang *et al.*,[51] are chosen based on physical aspects of the flow, rather than the mathematical bases and invariants of the strain and vorticity rate tensors. Table III shows these additional scalar features, highlighting parameters such as turbulent to mean kinetic energy ratio and the wall distance-based Reynolds number.

All the input features are constructed from suitable time-averaged parameters available in RANS. However, some parameters are not readily available in the time-averaged LES data. The velocity fields, resolved time-averaged turbulent kinetic energy and Reynolds stress fields are obtained directly from the LES. However, the specific turbulent dissipation rate and turbulent dissipation rate are not directly available from the LES data. To obtain the dissipation rates, the time-averaged LES field is frozen including the resolved turbulent kinetic energy, k. The transport equation for the k-ω SST[52] specific dissipation rate, ω, is solved iteratively over the frozen LES field. The transport model constants are consistent with those from Menter.[53] The approach enables functional predictions of turbulence dissipation and eddy viscosity. These predictions reflect the values that a RANS would calculate if the flow field and turbulent kinetic energy were identical to the LES.

D. Augmented RANS

A k-ω SST turbulence model is augmented with the turbulent anisotropy neural network model to improve the Boussinesq hypothesis Reynolds stresses available with a standard k-ω SST model in a RANS simulation. The RANS equations for continuity, momentum, and energy are solved using the *rhoSimpleFoam* pressure-based steady solver in OpenFOAM in the following forms, respectively:

$$\frac{\partial}{\partial x_j}(\bar{\rho}\bar{u}_j) = 0, \tag{12}$$

$$\frac{\partial}{\partial x_j}(\bar{\rho}\bar{u}_i\bar{u}_j) = -\frac{\partial \bar{P}}{\partial x_i} + \frac{\partial}{\partial x_j}\left(2\mu\bar{S}^*_{ij} - \bar{\rho}R_{ij}\right), \tag{13}$$

$$\frac{\partial}{\partial x_j}\left(\bar{\rho}\bar{u}_j\bar{h}_0\right) = \frac{\partial}{\partial x_j}\left(\bar{\rho}\alpha\frac{\partial \bar{h}}{\partial x_j} - \rho q_t\right), \tag{14}$$

where R_{ij} is the RANS Reynolds stresses and q_t is the RANS turbulent heat flux. In the present work, two closures for the turbulent heat flux are analyzed with the augmented model: the Gradient Diffusion Hypothesis (GDH) and the Higher-Order Generalized GDH (HOG) shown in Eqs. (15) and (16), respectively,

$$q_t^{GDH} = -\alpha_t\frac{\partial \bar{h}}{\partial x_i} = -\frac{\nu_t}{Pr_t}\frac{\partial \bar{h}}{\partial x_i}, \tag{15}$$

$$q_t^{HOG} = -c_\theta\tau_t\frac{R_{ik}R_{kj}}{k}\frac{\partial \bar{h}}{\partial x_j}. \tag{16}$$

The k-ω SST model is solved within the model, before augmenting with the turbulent anisotropy neural network model. The steady transport equations for turbulent kinetic energy, k, and specific turbulence dissipation rate, ω, are defined by Eqs. (17) and (18), respectively. The eddy viscosity, μ_t, used within the transport equations is defined by Eq. (19). The coefficients and blending are consistent with those published within Menter *et al.*,[53]

$$\frac{\partial \rho u_j k}{\partial x_j} = P_k - \beta^*\rho\omega k + \frac{\partial}{\partial x_j}\left[(\mu + \sigma_k\mu_t)\frac{\partial k}{\partial x_j}\right], \tag{17}$$

$$\frac{\partial \rho u_j \omega}{\partial x_j} = \frac{\gamma}{\nu_t}P_k - \beta\rho\omega^2 + \frac{\partial}{\partial x_j}\left[(\mu + \sigma_\omega\mu_t)\frac{\partial \omega}{\partial x_j}\right] + 2(1 - F_1)\frac{\rho\sigma_{\omega 2}}{\omega}\frac{\partial k}{\partial x_j}\frac{\partial \omega}{\partial x_j}, \tag{18}$$

$$\mu_t = \frac{a_1\rho k}{max(a_1\omega, \Omega F_2)}. \tag{19}$$

For the augmented SST model, OpenFOAM's *rhoSimpleFoam* operates as normal, progressing through momentum, energy, and pressure solvers before solving the turbulent equations at the end of the iteration. After the turbulence equations are solved, the neural network model is evaluated with the relevant input parameters to establish the turbulent anisotropy and Reynolds stresses for the next iteration. The neural network Reynolds stresses are obtained from the anisotropy output by the neural network model using Eq. (20), where the anisotropy directly output by the neural network is a_{ij}^{NN},

TABLE III. Additional normalized scalars for neural network input as used in studies Ling and Templeton[15] and Wang *et al.*[51]

ID	Description	Variable
p6	Ratio of turbulent kinetic energy to mean kinetic energy	$\frac{k}{k+0.5U_iU_i}$
p7	Ratio of turbulent timescale to mean strain-rate timescale	$\frac{\tau_t}{\tau_t+\frac{1}{\|\|S\|\|}}$
p8	Non-dimensional wall-distanced Reynolds number	$min\left(\frac{y\sqrt{k}}{50\nu},2\right)$
p9	Non-dimensional Q-criterion	$\frac{Q}{\|Q\|+\|\|S\|\|^2}$
p10	Pressure gradient along streamline	$\frac{U_k\frac{\partial P}{\partial x_k}}{\left\|U_k\frac{\partial P}{\partial x_k}\right\|+\sqrt{\frac{\partial P}{\partial x_j}\frac{\partial P}{\partial x_j}U_iU_i}}$
p11	Ratio of static pressure stress to dynamic pressure stress	$\frac{\sqrt{\frac{\partial P}{\partial x_i}\frac{\partial P}{\partial x_i}}}{\sqrt{\frac{\partial P}{\partial x_i}\frac{\partial P}{\partial x_i}}+\frac{1}{2}\rho\frac{\partial U_k}{\partial x_k}\frac{\partial U_k}{\partial x_k}}$
p12	Non-orthogonality between velocity vector and velocity gradient	$\frac{\lvert U_kU_l\frac{\partial U_k}{\partial x_l}\rvert}{\left\lvert U_iU_j\frac{\partial U_i}{\partial x_j}\right\rvert+\sqrt{U_nU_nU_i\frac{\partial U_i}{\partial x_j}U_m\frac{\partial U_m}{\partial x_j}}}$
p13	Ratio of convection to production of k	$\frac{U_i\frac{\partial k}{\partial x_i}}{\left\lvert U_i\frac{\partial k}{\partial x_i}\right\rvert+\lvert\overline{u_j'u_k'}S_{jk}\rvert}$
p14	Ratio of total to normal Reynolds stresses	$\frac{\|\|\overline{u_i'u_j'}\|\|}{\|\|\overline{u_i'u_j'}\|\|+k}$
p15	Streamline curvature	$\frac{\left\lvert\frac{D\Gamma}{Ds}\right\rvert}{\left\lvert\frac{D\Gamma}{Ds}\right\rvert+\frac{1}{L_c}}$
p16	Vortex stretching	$\frac{\sqrt{\omega_j\frac{\partial U_i}{\partial x_j}\omega_k\frac{\partial U_i}{\partial x_k}}}{\sqrt{\omega_l\frac{\partial U_n}{\partial x_l}\omega_m\frac{\partial U_n}{\partial x_m}}+\|\boldsymbol{S}\|}$
p17	Eddy-viscosity ratio	$\frac{\nu_t}{100\nu+\nu_t}$

$$R_{ij}^{NN}=2k\left(a_{ij}^{NN}+\frac{1}{3}\delta_{ij}\right). \tag{20}$$

Introducing full and accurate Reynolds stresses into the RANS momentum equations can be detrimental to the simulation's numerical stability. Explicit approaches can be ill-conditioned, particularly at high-Reynolds-number flows that are relevant in engineering applications.[54] Such behavior is common with RSTMs, where the coupling of velocity, pressure, and Reynolds stresses in the momentum equations can impede the stability and robustness of the model.[55]

TABLE IV. Dataset definitions showing the different combinations of training and validation datasets used to train neural network models in the present work.

	s35-br05-dr20	*l35-br10-dr20*	*m55-br10-dr16*
Set 1		✓	
Set 2	✓		✓
Set 3	✓	✓	✓

To improve the numerical robustness and stability of the augmented SST model, the modeled neural network Reynolds stress, R_{ij}^{NN}, is split into a linear and non-linear component. The linear component of the Reynolds stresses is equal to the Boussinesq hypothesis Reynolds stresses, where the eddy-viscosity type closure provides high numerical stability. This component has an implicit and explicit part within the segregated momentum equations. The non-linear component of the Reynolds stresses, τ_{ij}^{NL}, is the deficit between the neural network model and the Boussinesq hypothesis evaluated Reynolds stress tensor, shown in Eq. (21). This component is treated explicitly as an additional term within the momentum equation, highlighted by Eq. (22), where τ_{ij} is the deviatoric Reynolds stress. Such an approach was used by Wu *et al.*[54] on simple turbulent channel flow, periodic hills, and square duct flow, using a fully coupled momentum equation approach, allowing implicit treatment of the transposed velocity gradient term and an enhanced eddy viscosity to minimize the explicit non-linear component

$$R_{ij}^{NN} = \frac{2}{3}k\delta_{ij} + \tau_{ij}^{BH} + \tau_{ij}^{NL}, \tag{21}$$

$$\frac{\partial}{\partial x_j}(-\rho\tau_{ij}) = \overbrace{\underbrace{\frac{\partial}{\partial x_j}\left(\mu_t \frac{\partial \tilde{u}_i}{\partial x_j}\right)}_{\text{implicit}} + \underbrace{\frac{\partial}{\partial x_j}\left(\mu_t\left[\frac{\partial \tilde{u}_j}{\partial x_i} - \frac{2}{3}\frac{\partial \tilde{u}_k}{\partial x_k}\delta_{ij}\right]\right)}_{\text{explicit}}}^{\text{Boussinesq Hypothesis}} + \overbrace{\underbrace{\frac{\partial}{\partial x_j}\left(-\rho\sigma\tau_{ij}^{NL}\right)}_{\text{explicit}}}^{\text{Relaxed Non-linear Component}}. \tag{22}$$

For this complex, high-Reynolds number cases, the complexity of the equations and coupling of the velocity, pressure, Reynolds stresses, and additional turbulent terms, provide a highly coupled system of equations. A relaxation factor, σ, is introduced to the non-linear explicit Reynolds stresses in Eq. (22). Kaandorp and Dwight[56] introduced a blending factor between the Boussinesq hypothesis and full Reynolds stress components, allowing for highly anisotropic Reynolds stresses to be introduced while numerical stability and robustness was maintained. With the relaxation factor, the full neural network modeled Reynolds stresses are not used within the momentum equations and instead, a relaxed Reynolds stress tensor, R_{ij}^{mod}, shown in Eq. (23) is used in the momentum equation. The complete Reynolds stress tensor from the neural network model, R_{ij}^{NN}, is still available and can be used for other closures and visualization,

$$R_{ij}^{mod} = \frac{2}{3}k\delta_{ij} + \tau_{ij}^{BH} + \sigma\tau_{ij}^{NL}. \tag{23}$$

Furthermore, relaxation is also necessary in the near-wall region. Close to the wall, the anisotropy of the flow is high, providing a large non-linear component to the Reynolds stress in Eq. (22) that can negatively impact the solver if not appropriately addressed. Within this region, a parabolic damping function [Eq. (24)] is applied, providing a smooth transition across the near-wall region. The blending is a function of wall distance, d, where at the wall $\sigma_{local} = 0$. The blending is controlled by the parameter d^* that defines the near-wall distance where the blending is complete. For the present work, simulations with good stability and accuracy were found when the d^* was set to be just above the peak in near-wall anisotropy where the y^+ is between 100 and 120,

$$\sigma_{local} = min\left(\frac{d}{d^*}, 1\right)\left[2 - min\left(\frac{d}{d^*}, 1\right)\right]\sigma. \tag{24}$$

Since the neural network model provides local predictions of turbulent anisotropy, a_{ij}, based upon local features of the flow, smoothing is required to avoid spurious oscillations and discontinuities in the anisotropy field propagated to the solver. A box filter is used on the neural network anisotropy field to remove discontinuities. The filter is a surface integral of the interpolated face values of a field, shown by Eq. (25). The filter is applied to the neural network anisotropy field multiple times to produce a sufficiently smooth result. This approach is simple and efficient for unstructured finite volume codes. Multiple passes of a box filter can approximate a Gaussian filter.[57] It was found that 10 filtering iterations was suitable in the presented problems

TABLE V. Error of neural network model to LES resolved data compared for the two normalization approaches across the training and validation dataset sets defined in Table IV.

		Root mean square error (RMSE) error				
		Training and validation datasets			Testing datasets	
	No. of datasets	*s35-br05-dr20*	*l35-br10-dr20*	*m55-br10-dr16*	*s35-br10-dr20*	*m55-br04-dr16*
Set 1	1	0.068	0.048	0.101	0.055	0.067
Set 2	2	0.035	0.056	0.035	0.059	0.059
Set 3	3	0.033	0.038	0.036	0.042	0.043

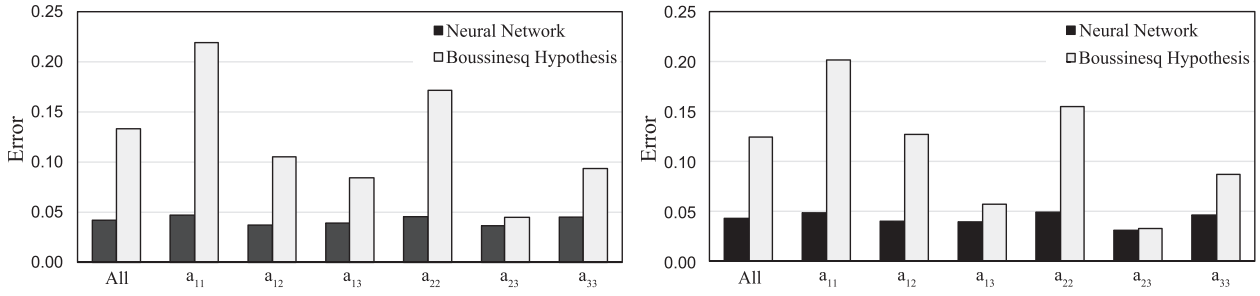

(a) *s35-br10-dr20* (b) *m55-br04-dr16*

FIG. 9. Comparing component-wise neural network error in anisotropy to the Boussinesq hypothesis model.

$$\tilde{\phi} = \frac{\sum_{i=1}^{N_{faces}} S_i \phi_i}{\sum_{i=1}^{N_{faces}} S_i}. \tag{25}$$

IV. RESULTS AND DISCUSSION

A. Anisotropy predictions

The present section details the initial *a priori* results. The LES data are used to train the neural network models, and its performance is then critiqued against the LES resolved anisotropy and Reynolds stresses. Within the initial results, three neural network models are investigated. Different arrangements of LES simulations used for the training and validation datasets are studied in three individual models. Table IV shows that LES simulations are investigated in three different sets.

Table V presents the raw *a priori* error for each LES dataset across the six trained neural network models. The error is defined here as the square root of the mean square difference between the neural network model and the resolved LES anisotropy data for the six unique components of the anisotropy tensor, shown by Eq. (26). The error results consider the blanking used for the neural network training, selecting datapoints where $k/U_\infty^2 > 0.0025$. This highlights the flow in the boundary layer, the separated regions, and the coolant jet where the improvements of the neural network model are critical,

$$Error = \sqrt{\frac{1}{6N}\sum_{n=1}^{N}\sum_{i=1}^{3}\sum_{j=i}^{3}\left(a_{ij}^{LES} - a_{ij}^{NN}\right)^2}. \tag{26}$$

Neural network models trained on Set 1, which included a single LES simulation *l35-br10-dr20* in the training and validation dataset, generally show the greatest error across all the studied models. However, it shows improved results across dataset *s35-br10-dr20*, a neighbor case where the blowing ratio, density ratio, and coolant hole inclination angle are equal. For case *m55-br10-dr16*, the response of the model is significantly worse than the other cases by a factor of 2. Although this case features jet lift-off, like *l35-br10-dr20*, the greater inclination angle of *m55-br10-dr16* provides a harsher lift-off condition that appears to produce a greater hurdle for the model compared to the attached conditions of *m55-br04-dr16*.

When training on datasets *s35-br05-dr20* and *m55-br10-dr16* (Set 2), Table V shows a larger error for the blanked dataset *s35-br10-dr20* than the models trained on Set 1. As the training datasets used are further distanced from dataset *s35-br10-dr20*, the increase in error is almost intuitive as the datasets used to train the model are less aligned to that dataset. A small reduction is seen for dataset *m55-br04-dr16*, but Table V shows that this is not significant, suggesting there is some coherence within the datasets that overlap with the data in *m55-br04-dr16*.

Table V demonstrates that the neural network model trained on Set 3, where the training and validation dataset is formulated from *s35-br05-dr20*, *l35-br10-dr20*, and *m55-br10-dr16*, shows reduced error for the blanked datasets *s35-br10-dr20* and *m55-br04-dr16*, and that the neural network was not trained upon. When considering the unblanked datasets, the diverse model shows marginally higher error than the models trained on Sets 1 and 2. The improvement seen in the untrained cases indicates that the model performance improves with the addition of diverse datasets. However, it comes at an increased computational cost of increased training times.

For the neural network model trained on Set 3, the local component-wise anisotropy error is summarized in Fig. 9 where both normalization strategies are compared to the Boussinesq hypothesis approach. Datasets *s35-br10-dr20* and *m55-br04-dr16* that were not featured in the training of the neural network models are presented and the discussed blanking is applied. The normal components offer the greatest improvement over the Boussinesq hypothesis. The off-diagonal components a_{12} and a_{13} exhibit large reductions in the anisotropy error where the neural network model reduces the error from 0.10 and 0.08 to 0.04, respectively. The a_{23} component shows a small improvement in *s35-br10-dr20* and no improvement in *m55-br04-dr16* but demonstrates that the neural network model equals or improves the anisotropy error of each component of the tensor across the cooling jets.

Contours of Reynolds stress components, derived from the neural network anisotropy, and anisotropy error are presented in Fig. 10 showing the *a priori* results of the neural network model for Set 3 on the untrained dataset *m55-br04-dr16*. It is noted that the stresses featuring a spanwise component are reflected across the centerplane, as expressed in Fig. 11, to easily compare the fields that would otherwise exhibit opposing polarities. This dataset shows good agreement between the LES and the neural network results for most of the components, with results that capture the near-wall peak in $\overline{u'u'}$. The local error of the anisotropy shows good success over much of the contour,

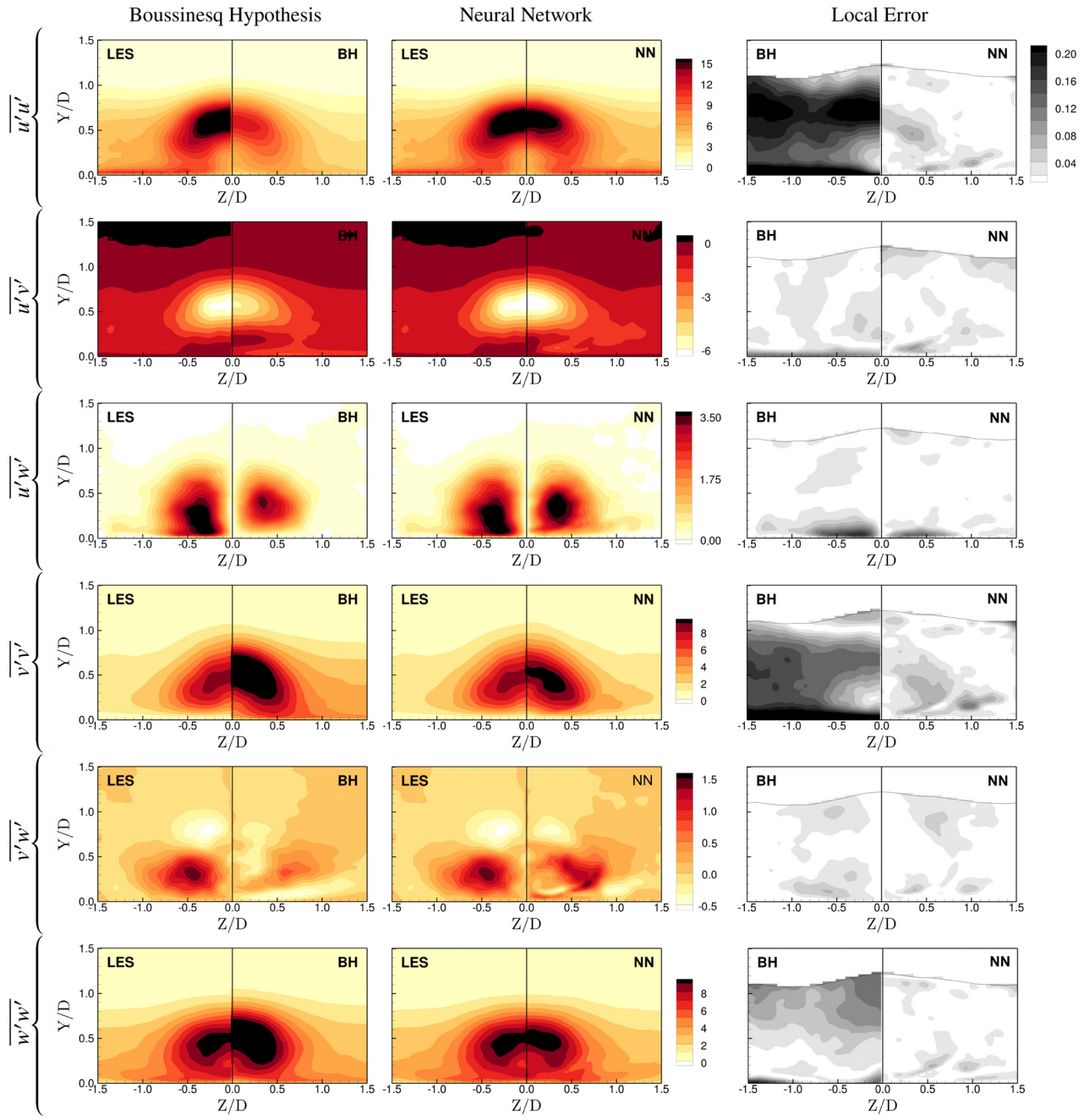

FIG. 10. Reynolds stress comparisons of the neural network model (Set 3) with specialized normalization and its local anisotropic error for case *m55-br04-dr16* across a spanwise slice at $X = 1D$.

with the largest improvements found in the normal components and also in the shear component adjacent to the wall. These results demonstrate the model can perform well on new datasets and provide improved Reynolds stresses, including the shear components, compared to the classic Boussinesq hypothesis approach used for most two-equation turbulence models.

The near-wall anisotropy can be compared with further clarity flow by assessing the anisotropic state using the barycentric or Lumley anisotropy maps. The barycentric maps are preferred over the Lumley maps because of the reduced bias toward any anisotropic state. Figure 12 displays the barycentric triangles with the anisotropic state modeled by the neural network for dataset *s35-br10-dr20* for three profiles

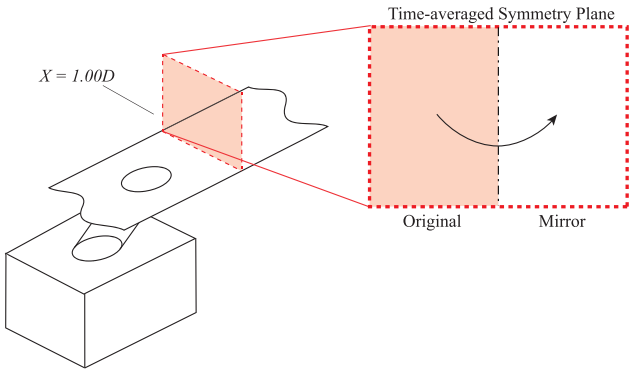

FIG. 11. Slice at $X = 1D$ with mirrored plane used for visualization and direct comparison of properties with spanwise velocities that would otherwise have opposing polarities across the centerplane.

across the jet centerplane, capturing the jet development and its changing anisotropic state. The neural network model predicts the expected near-wall behavior with an ascending anisotropy state from the two-component limit, replicating the LES data of all three profiles.

B. Augmented RANS predictions

Three cases are studied with the augmented RANS model. One of the cases, *s35-br10-dr20*, was evaluated in the *a priori* results of subsection IV A. Additionally, two cases are pursued to further investigate the performance of the model in cases that stray away from those the neural network model was trained on. Model case names are defined using Table VI, stating if the model uses the standard or neural network (NN) augmented SST model, using the neural network anisotropy, and if the model uses the GDH or HOGGDH turbulent heat flux closure.

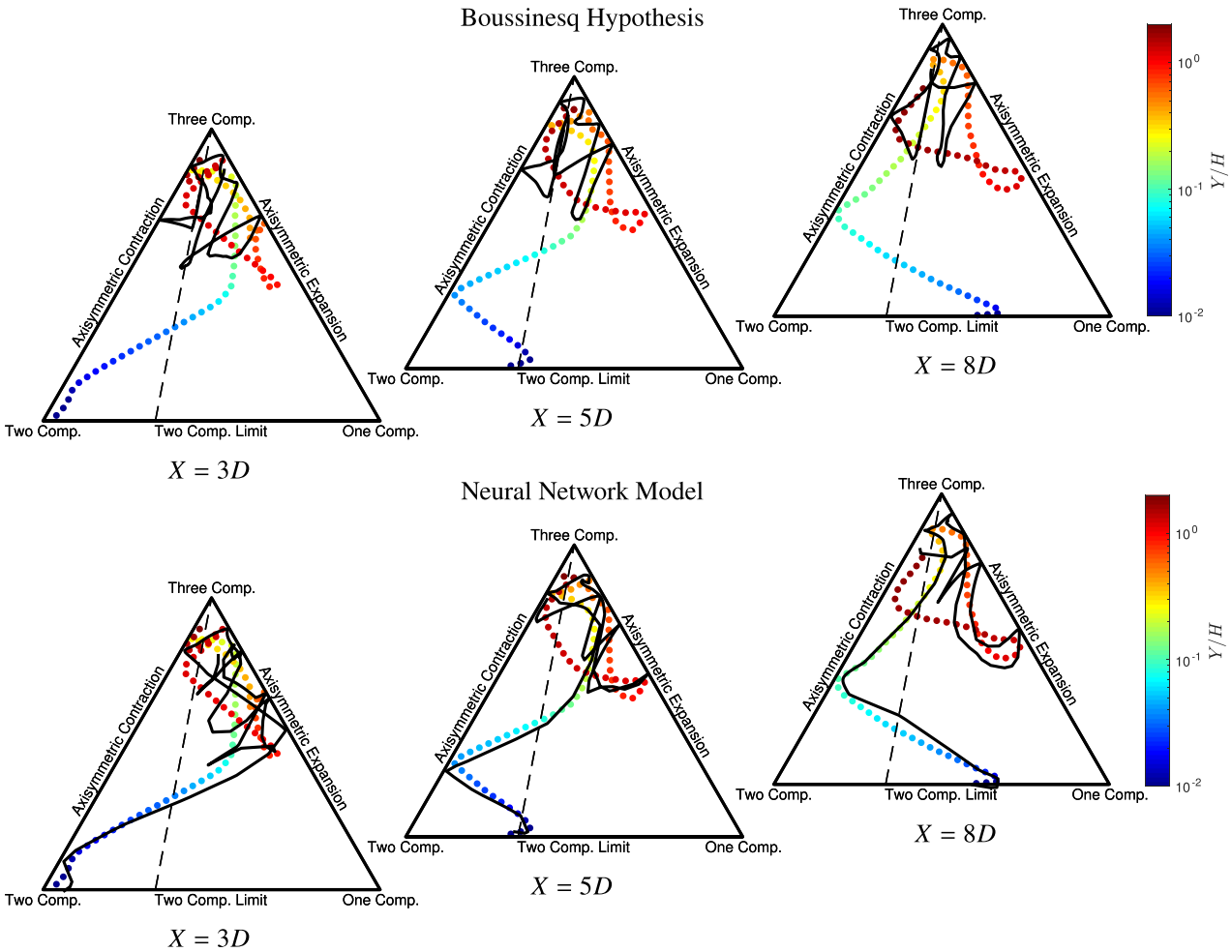

FIG. 12. Anisotropy results comparing the neural network models (trained on Set 3) on the testing case *s35-br10-dr20*.

TABLE VI. Case names and defining turbulence models and closures.

Case name	Model	$\overline{u_i'T'}$ closure
SST	Standard k-ω SST	...
SST-GDH		GDH
SST-HOG		HOGGDH
NNSST	NN augmented SST	...
NNSST-GDH		GDH
NNSST-HOG		HOGGDH

1. s35-br025-dr10

RANS augmentation results for the Reynolds stress neural network model are first investigated using the isothermal single-hole cooling case *s35-br025-dr10*. By assessing an isothermal case, the Reynolds stress results can be compared to the experiment without the interference of the turbulent heat flux closures, allowing a pure assessment of the Reynolds stress model on the RANS simulation. Experimental data for case *s35-br025-dr10* are provided in Pietrzyk *et al.*[25] and digitized for comparison in the present work.

Figure 13 shows the sum of the streamwise ($\overline{u'u'}$) and normal ($\overline{v'v'}$) Reynolds stress components and the shear stress component ($\overline{u'v'}$) compared between the standard and augmented SST model in the centerline profiles downstream of the cooling hole leading edge. Both plots show improved results of the augmented model, capturing the experimental peak in the shear layer at $X = 1D$, $2D$, and $3D$. However, the standard SST prediction improves the peak prediction of the turbulent shear stress at $X = 5D$.

At $X = 2D$, a strong near-wall peak is present in the standard k-ω SST results that is not present in the augmented model. This region lies outside the measured experimental profile but highlights the extreme difference between each model. The remainder of this profile shows the augmented model is in good agreement with the LES.

The results show a small snapshot of improvements to a couple of parameters, but begins to show the potential of such data-driven models in RANS settings. Furthermore, tests investigate the Reynolds stress, calculated from the data-driven anisotropy, and the flow's velocity and temperatures using the models, investigating the impact of the closure on the flow's principal variables.

2. s35-br10-dr20

The second test case used to assess the impact of augmentation in RANS simulations is the higher blowing ratio case *s35-br10-dr20*. This case has a density ratio (DR) of 2.0, introducing a temperature difference between the coolant and the mainstream flow. The augmented k-ω SST model with the neural network turbulent anisotropy (*NNSST*) is assessed using two turbulent heat flux closures: the GDH and HOGGDH.

Figure 14 compares the Reynolds stress results of the machine learning augmented SST model (*NNSST-HOG*) and the standard k-ω SST (*SST-HOG*) to those resolved by the LES. The upstream profile, $X = -2.75D$ (about $1D$ upstream of the coolant hole leading edge), shows the approaching turbulent boundary layer is well predicted by the augmented model, accurately capturing all Reynolds stress components and improving upon the standard SST predictions (*SST-HOG*) of the streamwise component R_{11}.

In the downstream profiles of Fig. 14, the augmented model improvements are present but lack the complete replication of the LES profiles. The improvements are still an achievement as one should be reminded of the complexity of mixing flows over turbulent boundary layers. The streamwise normal component above the cooling hole shows the augmented model predicts both the mixing shear layer peak and the larger peak at $X = -0.25D$ well. The greatest improvement of these predictions is in the peaks of the streamwise normal component, R_{11}, in the shear layer. The remaining components show small improvements over the standard SST model. In profiles $X \geq 1.25D$, between the shear layer peak and the wall, the results of both the standard and augmented SST models underpredict the normal components of the Reynolds stress tensor. This corresponds to an underprediction of the turbulent kinetic energy, k, in the discussed region. The machine learning model provides anisotropy to the augmented SST and relies upon the transport equations of the SST model to provide the turbulent kinetic energy.

With improvements identified in the Reynolds stress predictions, the impact of the augmented model on the flowfield is sought by assessing the streamwise and normal velocity profiles in Fig. 15. Both the standard and augmented SST models show similar profiles with the same trends. Small differences are present between the contrasting models, the most noticeable of which is in the non-dimensional normal velocity (V/U_∞) profiles. The augmented model suppresses the

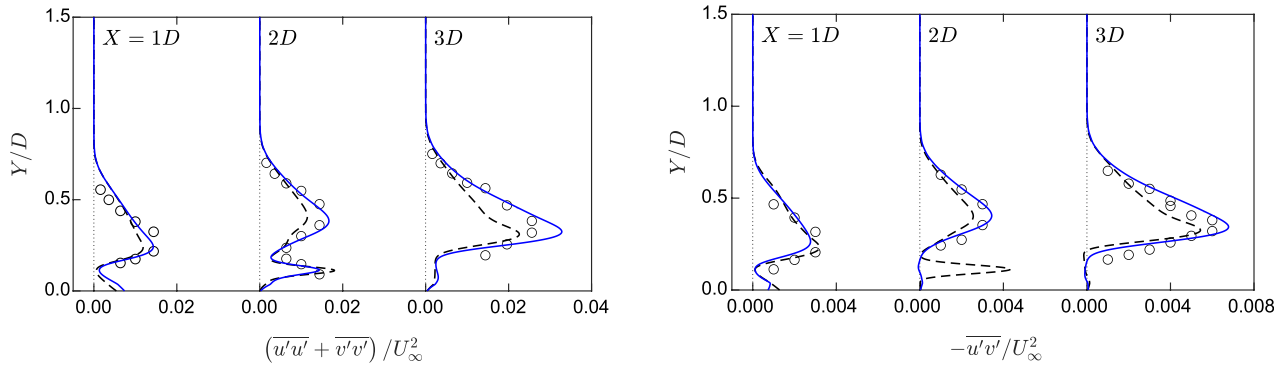

FIG. 13. Comparison of turbulent normal and shear stresses of the standard SST (*SST*) (black dashed line), the augmented NN SST model (*NNSST*) [blue line], and the experimental measurements[25] (open circle).

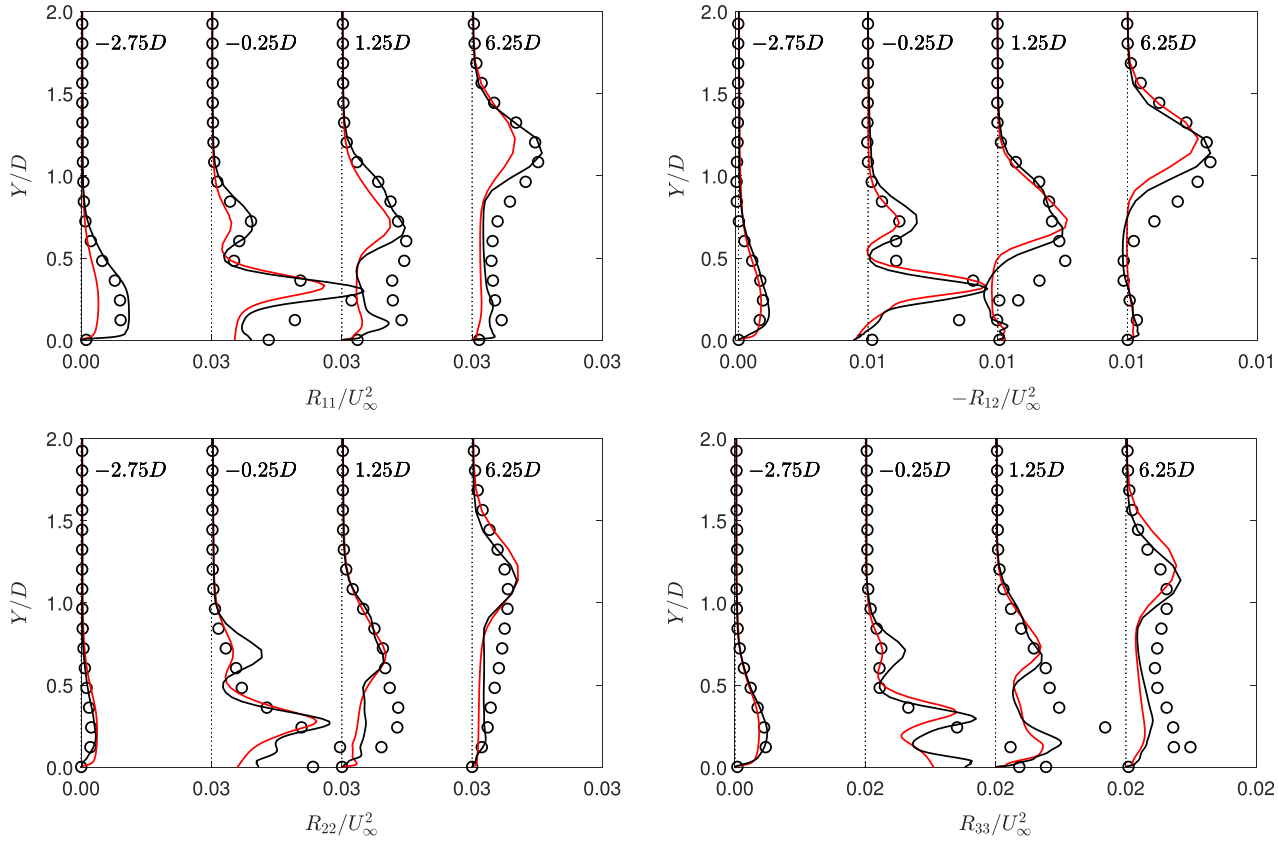

FIG. 14. Comparing Reynolds stress results in centerline profiles for cases *SST-HOG* [red line] and the augmented model *NNSST-HOG* (black line) with the LES resolved Reynolds stresses (open circle).

normal velocity of the jet, which will reduce the coolant vertical penetration into the hot mainstream. In the profiles of streamwise velocity, the augmented model shifts the velocity profile closer to those of the time-averaged LES, indicating a positive impact of including realistic anisotropy in RANS simulation with neural network models.

The augmented model is run for case *s35-br10-dr20* with the GDH and HOGGDH models. Non-dimensional temperature centerline profiles of the two models are compared in Fig. 16. Results show the GDH closure with the augmented model captures the LES data in the early development of the jet $X \leq 1.25$, correctly predicting the initial mixing on the centerline, whereas the HOGGDH approach shows

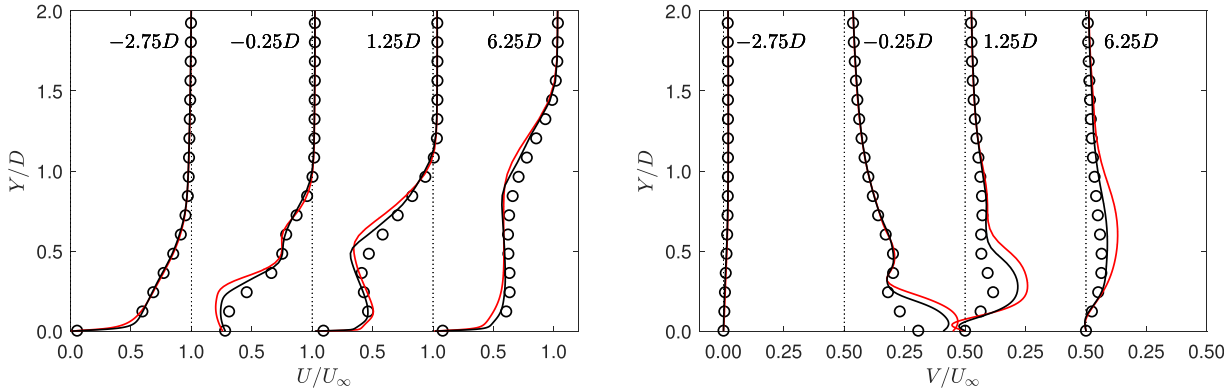

FIG. 15. Comparing centerline velocity profiles from the standard *SST-HOG* model [red line] and the augmented model *NNSST-HOG* (black line) to the LES data (open circle).

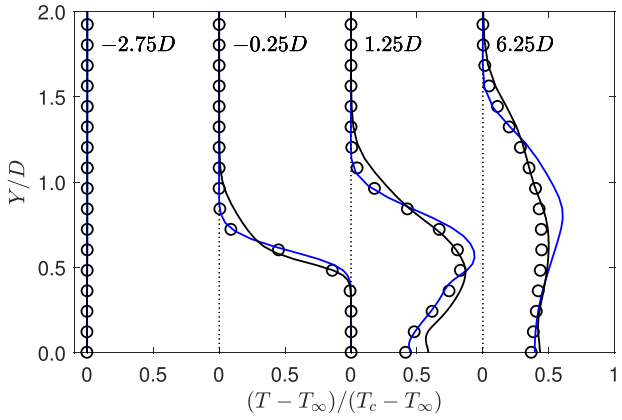

FIG. 16. Non-dimensional temperature profiles of augmented simulations with GDH (*NNSST-GDH*) [blue line] and HOGGDH (*NNSST-HOG*) (black line) compared to the time-averaged LES profiles (open circle).

increased diffusion in the shear layer. In the downstream centerline profiles of Fig. 16, the HOGGDH model shows improvements over the GDH approach, capturing the diffused temperature profile, while the GDH closure exhibits a distinct peak remaining from the shear layer. The comparison of the closures highlights the further work needed for turbulent heat flux closures that improve the temperature profile for the initial jet development as well as the downstream hot-cold gas mixing that is improved with the HOGGDH turbulent heat flux closure.

Furthermore, temperature predictions are assessed by investigating the wall ACE. The ACE is extracted and compared between the discussed augmented simulations with GDH and HOGGDH closures and compared to respective standard SST models in Figs. 17 and 18. The GDH approach with the augmented model shows improved wall ACE over the standard k-ω SST model with GDH closure. As shown in the results of Fig. 16, the augmented model with GDH improves the early jet development region, providing good predictions of lateral and centerline ACE distributions up to $X = 5D$. The centerline predictions then remain close to the LES results across the downstream region. However, the spanwise-averaged ACE is underpredicted as less lateral coolant spreading is provided by the GDH closure. The standard k-ω SST approach fails to capture the ACE trends and values across the flow.

The wall ACE results of the augmented model with the HOGGDH closure are compared in Fig. 18. The standard k-ω SST model with HOGGDH closure shows a good estimation of the LES time-averaged ACE. The centerline trend is better captured than that of the augmented model, but the standard approach overpredicts the centerline ACE. Downstream, the ACE centerline and lateral distributions are well predicted by the augmented model, as shown in the results of Fig. 16, accurately capturing the time-averaged ACE of the LES. Results of the augmented model with GDH and HOGGDH closures show the augmented model accurately captures the early jet development region close to the trailing edge of the cooling hole and the HOGGDH closure improves the downstream behavior. In these regions, the augmented approach improves the predicted wall ACE over the standard SST model, but a need for advanced turbulent heat flux closure developments is necessary for further flow improvements.

Figure 19 shows the contours of ACE across the coolant plate, which provides additional detail not easily observed in Figs. 17 and 18. The results indicate the improved flow field provided by the augmented model with neural network anisotropy. Downstream of the coolant hole, the standard SST model presents a distinguished peak in the ACE distribution, $0.5D$ from the centerline. This peak is not exhibited in the LES. Additionally, the LES shows a large cooling effectiveness immediately aft of the cooling hole trailing edge that is not present in the standard SST data. Introducing the augmented model provides the increased cooling effectiveness present aft of the trailing

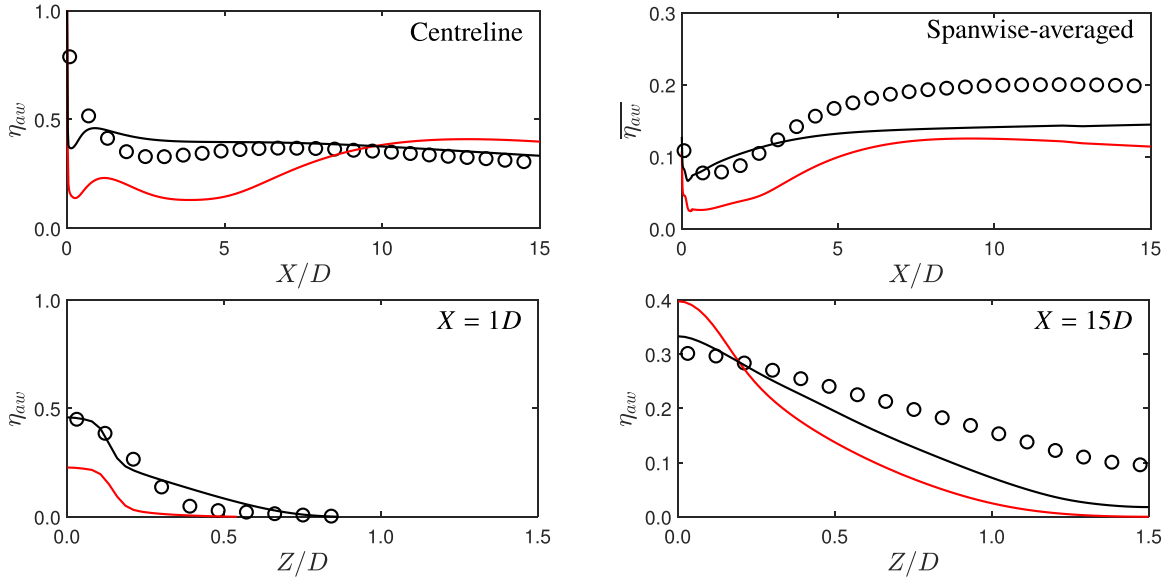

FIG. 17. ACE comparison of the NN augmented SST (black line) and standard SST model [red line] using the GDH closure to LES data (open circle).

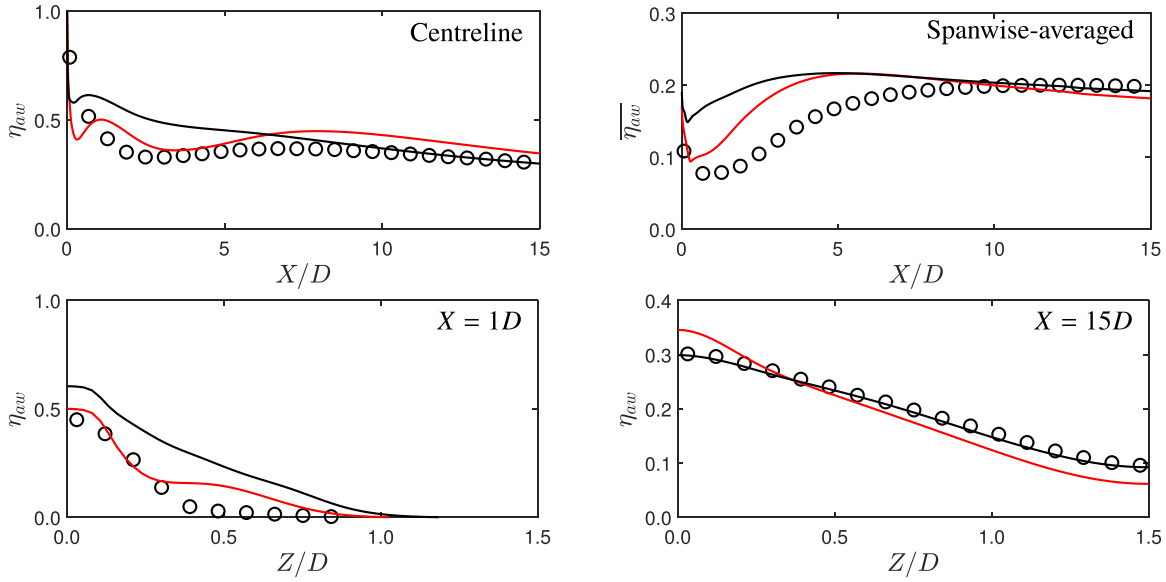

FIG. 18. ACE comparison of the NN augmented SST (black line) and standard SST model [red line] using the HOGGDH closure to LES data (open circle).

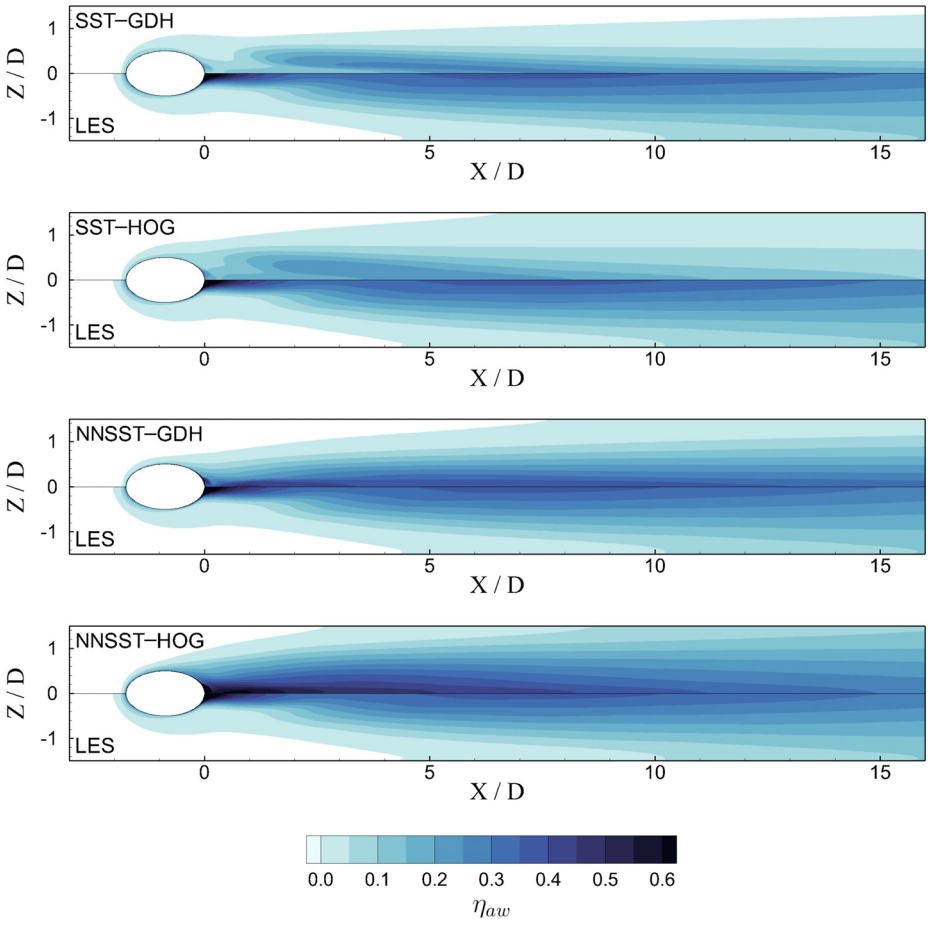

FIG. 19. Contours of ACE across the downstream plate comparing standard to augmented NN SST models with the GDH and HOGGDH turbulent heat flux models.

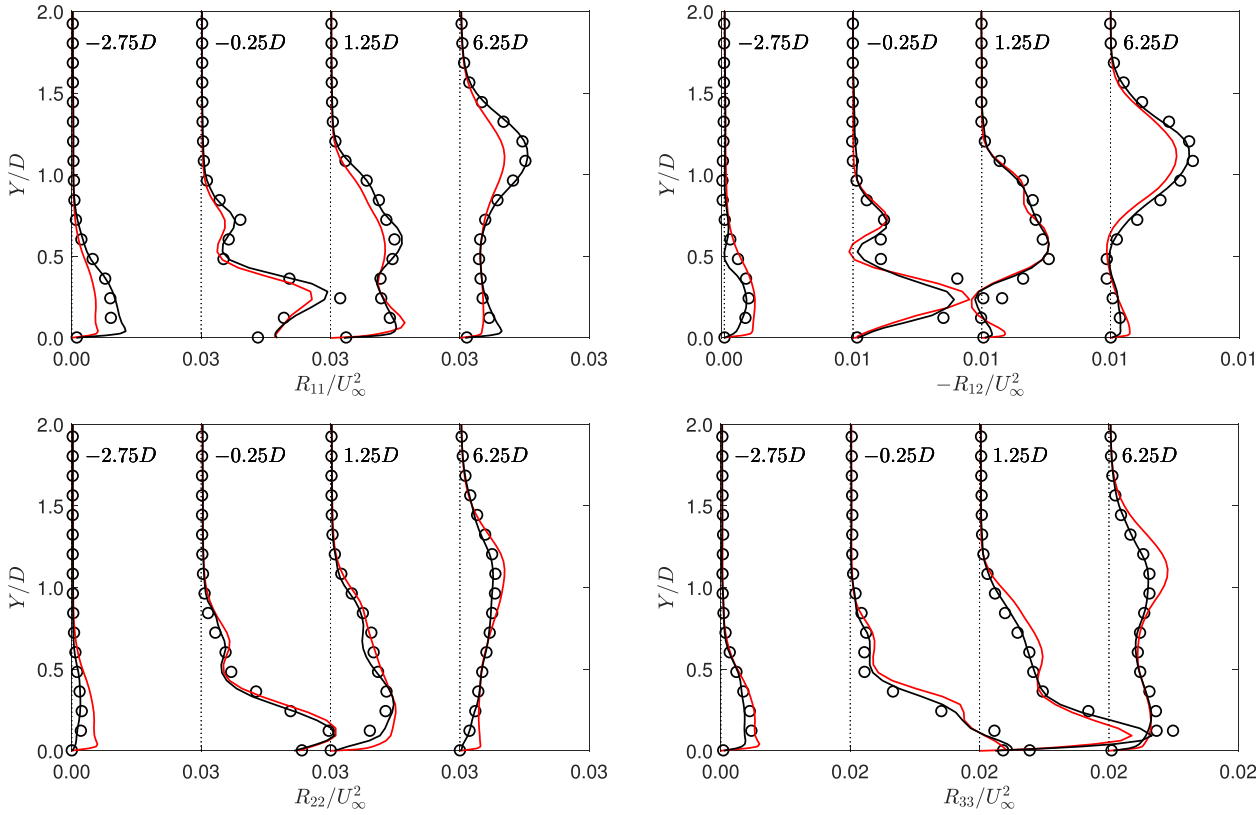

FIG. 20. Comparisons of Reynolds stress centerline profiles across simulations with a LES frozen *k* field. *SST-kLES* [red line], *NNSST-kLES* (black line), and LES resolved data (open circle).

edge and does not show the unphysical peak in ACE exhibited by the standard SST model. Increases in the lateral spreading rate in coolant are evident in the models using the HOGGDH turbulent heat flux closure; however, this overestimates the lateral distribution in the early development of the cooling jet (also shown in Fig. 18). A compromise between the two turbulent heat flux models would be favorable.

The earlier augmented model results showed an underprediction of turbulent kinetic energy in the near-wall region of the centerline profiles downstream of the cooling hole trailing edge. Augmenting RANS models with machine learnt anisotropy does not directly impact the flow's turbulent kinetic energy and relies upon the underlying predictions of the base turbulence model (the SST model has been investigated in the present studies). To address the improvements of the augmented model, when an accurate turbulent kinetic energy field is present, simulations are performed and analyzed with a frozen turbulent kinetic energy field taken from the respective LES (*SST-kLES* and *NNSST-kLES*).

Figure 20 replicates the previous centerline profiles of Reynolds stress for the frozen field cases. With the frozen turbulent kinetic energy field, the machine learning augmented RANS improves the Reynolds stress predictions in the region between the shear layer and the near-wall in the downstream profiles, which were shown to be underpredicted when the pure augmented model was assessed in Fig. 15. The results of the augmented model closely match the LES resolved stresses and show the improvement in Reynolds stress results with a neural network model of full turbulence anisotropy. Minor differences are presented in the upstream turbulent shear stress profile, where the standard SST model shows a closer trend to that observed by the LES.

Off-centerline profiles of Reynolds stresses are further shown in Fig. 21 and highlight similar agreements as illustrated by the centerline profiles. Achieving good predictions in the lateral, off-centerline positions is critical in reproducing the correct lateral spreading behavior of coolant jets. In the off-centerline profiles, a greater difference between the standard k-ω SST model and the augmented model is observed. The results show the linear anisotropy behavior underpredicts the streamwise component of Reynolds stress, R_{11}, while overestimating the normal component, R_{22}. However, the neural network model of turbulent anisotropy provides an accurate Reynolds stress tensor in the off-centerline profiles, when provided with an accurate turbulent kinetic energy field.

The anisotropic state of turbulence with the frozen field simulations is shown using barycentric triangles in Fig. 22 across three centerline profiles. With the improved Reynolds stress predictions from frozen LES resolved turbulent kinetic energy field shown in the centerline profiles (Fig. 20), the barycentric plots show an improved agreement with the LES resolved anisotropy. With accurate Reynolds stresses captured away from the wall with the frozen LES turbulent kinetic energy field, the near-wall discrepancy shown by the

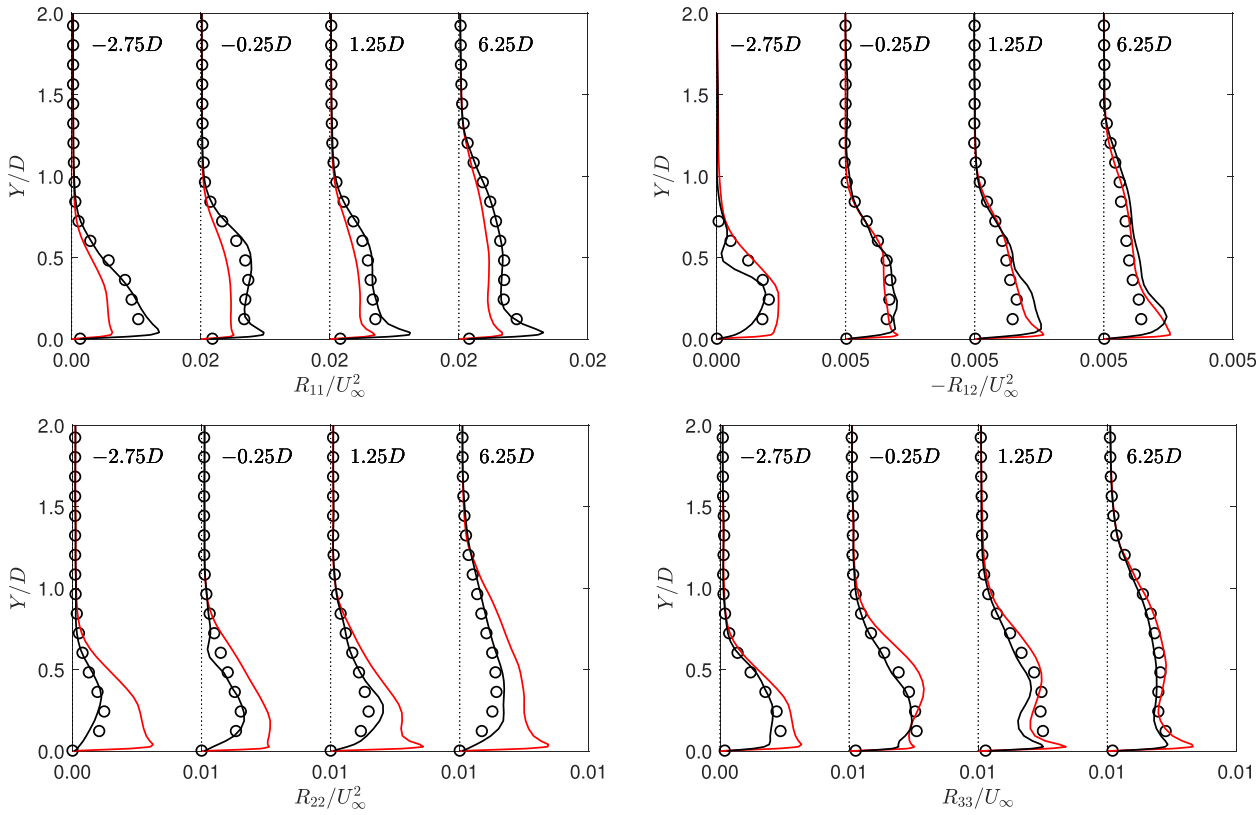

FIG. 21. Comparisons of off-centerline ($Z = 1D$) velocity profiles across simulations with a LES frozen k field. *SST-kLES* [red line], *NNSST-kLES* (black line), and LES resolved data (open circle).

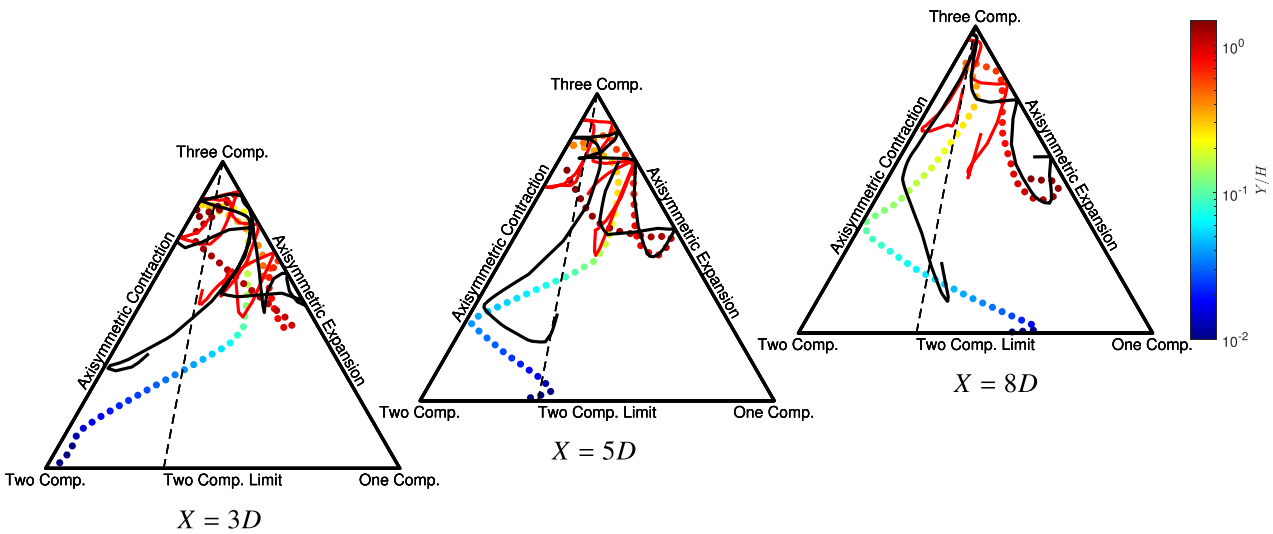

FIG. 22. Anisotropy plots from frozen LES field simulations. *SST-kLES* [red line], *NNSST-kLES* (black line), and LES resolved data (dots).

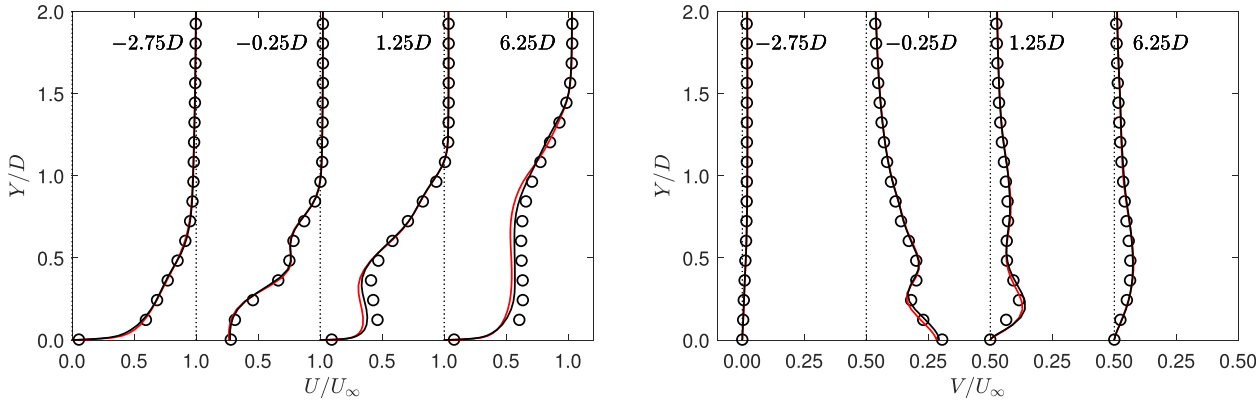

FIG. 23. Comparisons of centerline velocity profiles across simulations with a LES frozen *k* field. *SST-kLES* [red line], *NNSST-kLES* (black line), and LES resolved data (open circle).

barycentric triangles confirms the deviation is driven by the filtering procedure.

As accurate predictions of Reynolds stress components are found when the augmented model is used with an LES frozen turbulent kinetic energy field, velocity fields are examined to assess the impact of "near-perfect" Reynolds-stress predictions from the neural network model. Profiles of streamwise and normal velocity centerline profiles are shown in Fig. 23. It should be noted that the Reynolds stresses seen in the momentum transport equations are the relaxed stresses derived from the full stresses, which is necessary for numerical stability.

Results of the velocity centerline profiles (Fig. 23) show similar trends and results in all three cases, including the standard SST model with a frozen turbulent kinetic energy field, which is in good agreement with the LES time-averaged velocities. Small improvements are shown in the streamwise velocity in profiles $X = 1.25D$ to $6.25D$. These results indicate that the improved anisotropy available with an augmented neural network model provides some improvements in the centerline velocity profiles and the biggest improvements are found by coupling the neural network model of anisotropy with improvements to the turbulent kinetic energy predictions. However, the augmented model has clear benefits in the temperature field as shown by the ACE predictions of Figs. 17 and 18. Additionally, the deviation from the anisotropic two-component limit state does not negatively impact the flow's velocity field.

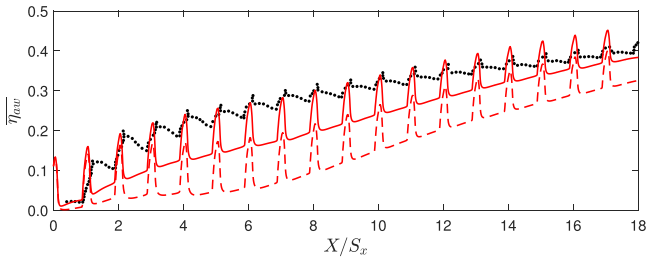

(a) *SST-GDH* [- · -] and *NNSST-GDH* [—].

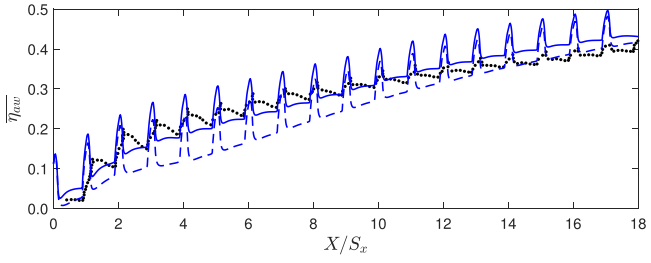

(b) *SST-HOG* [- - -] and *NNSST-HOG* [—].

FIG. 24. Spanwise-averaged ACE for the multi-hole cooling array case compared to experimental datasets[58] (black dot).

3. Multi-hole

A final investigation has been performed on a multi-hole effusion cooling array, investigated both experimentally and numerically by Andrei *et al.*[58] Results of their paper showed numerical results using local isotropic modifications to improve the coolant transport predictions. Results showed good agreement with experimental data for very high blowing ratios ($BR \geq 2$) but struggled to predict ACE distributions at a $BR = 1$ with $DR = 1.5$ which we numerically investigate here. Four CFD simulations are presented covering the augmented Reynolds stress and turbulent heat flux models (outlined in Table VI) to demonstrate the impact on model predictions.

Spanwise-averaged ACE results are shown in Fig. 24 comparing the experimental dataset of Andrei *et al.*[58] The classic SST model with the GDH approach found in out-of-the-box CFD packages shows large under predictions in the ACE across the plate. This approach demonstrates a step change at $X = 6S_x$ that is not present in the experimental dataset. Introducing the neural network anisotropy in the augmented SST model into the simulation with the GDH closure begins to improve the results, removing the step change exhibited by the standard SST model. Use of the HOGGDH closure improves the flow further [Fig. 25(b)], showing the additional complexity of the HOGGDH coupled with the augmented NN SST model matches the trends of the experiment and closely replicates the spanwise-averaged values.

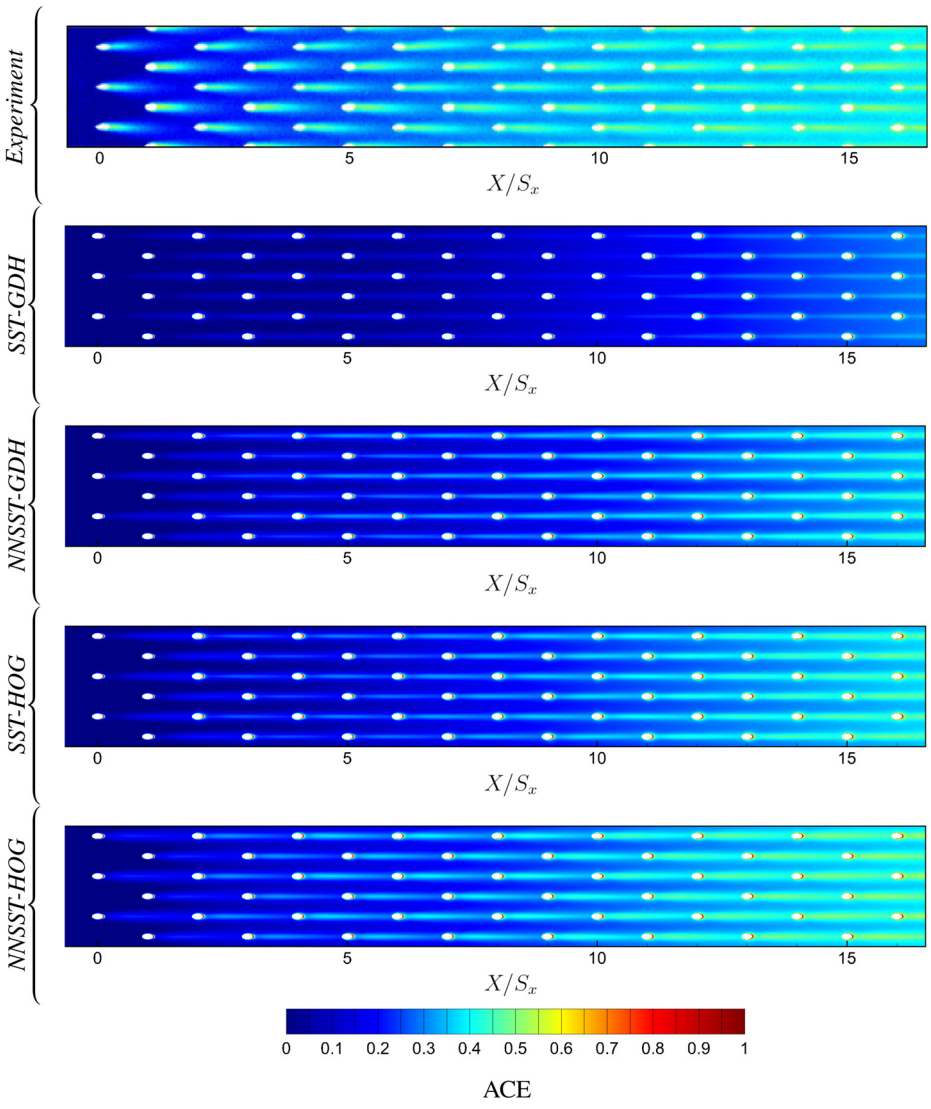

FIG. 25. Plate ACE contour comparisons of the multi-hole cooling array case.

The augmented turbulent heat flux coefficient is introduced in Fig. 24(c) and shows similar behavior to the GDH and HOGGDH results when the augmented Reynolds stress model is used. In the downstream flow ($X > 14S_x$), the spanwise-averaged results are well predicted by the augmented model, but earlier in the flow, the HOGGDH closure, with a constant c_θ of 0.6, provides a better representation of the flow.

ACE contours across the effusion cooling plate produce a richer description of the coolant behavior between the models studied in Fig. 25. The underprediction of the GDH shown in Fig. 24 demonstrates small amounts of the coolant entrain at the plate surface. Case *NNSST-GDH* shows improvements but the lateral spreading of the coolant does not reflect the spreading shown in the experimental contours and the coolant is mostly confined to a small hypothetical channel downstream of each coolant hole. Introducing the HOGGDH improves the lateral spreading as expected and the *NNSST-HOG* results show a qualitative similarity to the experimental contour published by Andrei *et al.*[58] in the downstream region ($X > 10S_x$). Over the initial holes, the experiment exhibits a greater degree of coolant distribution at the wall directly aft of each coolant hole.

V. CONCLUSIONS

The paper has shown an implementation of the TBNN in order to provide an advanced closure to the Reynolds stress tensor for two-equation turbulence models. The selection of invariants and novel parameters provides a diverse input space for use in the neural network model that can be combined with the tensor inputs and used within the TBNN framework that is mathematically underpinned by Pope.[50] The research conclusions can be summarized by the following points:

- The neural network approach vastly improved the Reynolds stress and anisotropic state over the Boussinesq hypothesis approach used in standard two-equation turbulence models.

Results show improvements on all anisotropy components across cooling cases not featured in the training and validation datasets.
- When demonstrated in a RANS environment with a k-ω SST model, the TBNN model provides improvements to Reynolds stress fields. These improvements were exhibited in different cooling cases showing improvements to velocity and temperature fields as a consequence of the improved Reynolds stress field contributed by the neural network model.
- Using the augmented model with the GDH and HOGGDH results showed improved ACE distributions. However, the GDH model still underpredicted the lateral coolant spread, while the HOGGDH model provided an overprediction. An improved turbulent heat flux model should be sought in future work.
- A frozen LES turbulent kinetic energy field used with the model, to improve the underpredictions in the field, provided the reproduction of Reynolds stresses and further improved the velocity field modeled. This indicates improvements to not just the turbulent anisotropy field are important but the predicted turbulent kinetic energy field is a critical factor and should be sought in future data-driven models.
- An additional case that investigated multi-row effusion cooling, that further distances itself from the training datasets, was performed at conditions that proved difficult for previous simulations[58] to replicate. Results showed the machine learnt turbulence anisotropy improved the agreement of the cooling distribution to the experimental data and the best comparisons were made when the HOGGDH turbulent heat flux model was employed.

Using machine learning methods for improving an existing turbulence model has provided a strategy that captures the physics of film and effusion cooling flows that is not found in the original turbulence model.

ACKNOWLEDGMENTS

C. D. Ellis is supported by the EPSRC Centre for Doctoral Training in Gas Turbine Aerodynamics (Grant No. EP/L015943/1). The authors would like to acknowledge the use of Athena at HPC Midlands+, which was funded by the EPSRC (Grant No. EP/P020232/1).

NOMENCLATURE

a_{ij}	Anisotropy Tensor
d	Wall-distance (m)
D	Coolant Hole Diameter (m)
G	Coefficient
k	Turbulent Kinetic Energy (m^2/s^2)
l	Coolant Hole Length (m)
L	Length Scale (m)
p	Pitch (m) / Scalar Feature
P	Pressure (Pa)
q_t	Turbulent Heat Flux (m^2/s^3)
Re_j	Coolant Jet Reynolds Number
r_k	Ratio of Resolved-Total Turbulent Kinetic Energy
R_{ij}	RANS Reynolds Stress Tensor (m^2/s^2)
S	Face Area (m^2)
s_{ij}	Normalised Strain-rate Tensor
S_{ij}	Strain-rate Tensor ($1/s$)
T	Temperature (K) / Tensor Feature
u_i/U	Velocity (m / s)
u_τ	Friction Velocity (m / s)
$\overline{u_i'u_j'}$	LES Reynolds Stress Tensor (m^2/s^2)
w_{ij}	Normalised Vorticity Tensor
W_{ij}	Vorticity Tensor ($1/s$)
x / X	X Coordinate (m)
y / Y	Y Coordinate (m)
z / Z	Z Coordinate (m)

Greek Symbols

α	Inclination Angle ($^\circ$) / Diffusivuty (m^2/s)
δ_{ij}	Identity Matrix
ϵ	Turbulence Dissipation Rate (m^2/s^3)
η_{aw}	Adiabatic Cooling Effectiveness
λ	Coefficient
μ	Dynamic Viscosity ($kg/m/s$)
ν	Kinematic Viscosity (m^2/s)
ρ	Density (kg/m^3)
σ	Blending Coefficient
τ_{ij}	Deviatoric Stress Tensor (m^2/s^2)
τ_t	Turbulent Time Scale (s)
ω	Specific Turbulence Dissipation Rate ($1/s$)
ω_i	Vorticity vector ($1/s$)

Subscripts

$\square_c$	Coolant Property
$\square_{res}$	Resolved Property
$\square_{rms}$	Root-Mean-Square
$\square_{sgs}$	Sub-grid Scale Property
$\square_t$	Turbulent Property
$\square'$	Fluctuating Property
$\square_\infty$	Freestream Property

Abbreviations

ACE	Adiabatic Cooling Effectiveness
BH	Boussinesq Hypothesis
BR	Blowing Ratio
DR	Density Ratio
DNS	Direct Numerical Simulation
GDH	Gradient Diffusion Hypothesis
GEP	Gene Expression Programming
HOGGDH	Higher-Order Generalised Gradient Diffusion Hypothesis
LES	Large-Eddy Simulation
NN	Neural Network
RANS	Reynolds-Averaged Navier-Stokes
RMSE	Root-Mean Square Error
RSTM	Reynolds-Stress Transport Model
SST	Shear Stress Transport
TBNN	Tensor-Basis Neural Network
WALE	Wall-Adaptive Local Eddy viscosity

AUTHOR DECLARATIONS

Conflict of Interest

The authors have no conflicts to disclose.

Author Contributions

Christopher D. Ellis: Conceptualization (equal); Data curation (equal); Formal analysis (equal); Investigation (equal); Methodology (equal); Resources (equal); Validation (equal); Visualization (equal); Writing – original draft (equal); Writing – review & editing (equal). **Hao Xia:** Conceptualization (equal); Project administration (equal); Resources (equal); Supervision (lead); Writing – review & editing (equal).

DATA AVAILABILITY

The data that support the findings of this study are available from the corresponding author upon reasonable request.

REFERENCES

[1]C. D. Ellis and H. Xia, "Turbulent closure analysis in heated separated and reattached flow using eddy-resolving data," Phys. Fluids **32**, 045115 (2020).
[2]K. Duraisamy, Z. J. Zhang, and A. P. Singh, "New approaches in turbulence and transition modeling using data-driven techniques," AIAA Paper No. 2015-1284, 2015.
[3]A. Hoda and S. Acharya, "Predictions of a film coolant jet in crossflow with different turbulence models," J. Turbomach. **122**, 558–569 (2000).
[4]S. Acharya, M. Tyagi, and A. Hoda, "Flow and heat transfer predictions for film cooling," Ann. N. Y. Acad. Sci. **934**, 110–125 (2001).
[5]D. K. Walters and J. H. Leylek, "A systematic computational methodology applied to a three dimensional film-cooling flowfield," in International Gas Turbine and Aeroengine Congress and Exhibition (1996).
[6]D. K. Walters and J. H. Leylek, "A detailed analysis of film-cooling physics Part 1: Streamwise injection with cylindrical holes," in International Gas Turbine and Aeroengine Congress and Exhibition (1997).
[7]K. L. Harrison and D. G. Bogard, "Comparison of RANS turbulence models for prediction of film cooling performance," ASME Turbo Expo: Power Land, Sea, Air **43147**, 1187–1196 (2008).
[8]A. Azzi and B. A. Jubran, "Numerical modeling of film cooling from short length stream-wise injection holes," Heat Mass Transfer **39**, 345–353 (2003).
[9]G. Bergeles, A. D. Gosman, B. E. Launder, and G. Bergeles, "The turbulent jet in a cross stream at low injection rates: A three-dimensional numerical treatment," Numer. Heat Transfer **1**, 217–242 (1978).
[10]M. Tyagi and S. Acharya, "Large eddy simulation of film cooling flow from an inclined cylindrical jet," J. Turbomach. **125**, 734–742 (2003).
[11]P. Renze, W. Schroder, and M. Meinke, "Large-eddy simulation of film cooling flows with variable density jets," Flow, Turbul. Combust. **80**, 119–132 (2008).
[12]P. Renze, W. Schroder, and M. Meinke, "Large-eddy simulation of film cooling flows at density gradients," Int. J. Heat Fluid Flow **29**, 18–34 (2008).
[13]J. Bodart, F. Coletti, I. Bermejo-Moreno, and J. K. Eaton, "High-fidelity simulation of a turbulent inclined jet in a crossflow," in *Center for Turbulence Research* (Stanford University, 2013), pp. 263–275.
[14]C. Ellis and H. Xia, "Impact of inflow turbulence on large-eddy simulation of film cooling flows," Int. J. Heat Mass Transfer **195**, 123172 (2022).
[15]J. Ling and J. Templeton, "Evaluation of machine learning algorithms for prediction of regions of high Reynolds averaged Navier–Stokes uncertainty," Phys. Fluids **27**, 085103 (2015).
[16]J. Ling, A. Kurzawski, and J. Templeton, "Reynolds averaged turbulence modelling using deep neural networks with embedded invariance," J. Fluid Mech. **807**, 155 (2016).
[17]Y. F. Marioni, E. A. de Toledo Ortiz, A. Cassinelli, F. Montomoli, P. Adami, and R. Vazquez, "A machine learning approach to improve turbulence modelling from DNS data using neural networks," Int. J. Turbomach., Propul. Power **6**, 17 (2021).
[18]J. Weatheritt and R. Sandberg, "A novel evolutionary algorithm applied to algebraic modifications of the RANS stress-strain relationship," J. Comput. Phys. **325**, 22–37 (2016).
[19]J. Weatheritt and R. D. Sandberg, "The development of algebraic stress models using a novel evolutionary algorithm," Int. J. Heat Fluid Flow **68**, 298–318 (2017).
[20]P. M. Milani, J. Ling, G. Saez-Mischlich, J. Bodart, and J. K. Eaton, "A machine learning approach for determining the turbulent diffusivity in film cooling flows," J. Turbomach. **140**, 021006 (2017).
[21]P. M. Milani, J. Ling, and J. K. Eaton, "Turbulent scalar flux in inclined jets in crossflow: Counter gradient transport and deep learning modelling," arXiv:2001.04600 (2020).
[22]J. Ling, A. Ruiz, G. Lacaze, and J. Oefelein, "Uncertainty analysis and data-driven model advances for a jet-in-crossflow," in *Proceedings of Turbo Expo: Power for Land, Sea, and Air* (ASME, 2016), Paper No. GT2016-56191.
[23]C. D. Ellis, H. Xia, and G. J. Page, "LES informed data-driven modelling of a spatially varying turbulent diffusivity coefficient in film cooling flows," in *Proceedings of Turbo Expo: Power for Land, Sea, and Air* (American Society of Mechanical Engineers, 2020), Vol. 84171, p. V07BT12A029.
[24]A. K. Sinha, D. G. Bogard, and M. E. Crawford, "Film-cooling effectiveness downstream of a single row of holes with variable density ratio," J. Turbomach. **113**, 442–449 (1991).
[25]J. R. Pietrzyk, D. G. Bogard, and M. E. Crawford, "Effects of density ratio on the hydrodynamics of film cooling," in Proceedings of Turbo Expo: Power for Land, Sea and Air, Volume 4: Heat Transfer; Electric Power; Industrial and Cogeneration (1989).
[26]J. R. Pietrzyk, D. G. Bogard, and M. E. Crawford, "Hydrodynamic measurements of jets in crossflow for gas turbine film cooling applications," J. Turbomach. **111**, 139–145 (1989).
[27]A. Kohli and D. G. Bogard, "Adiabatic effectiveness, thermal fields, and velocity fields for film cooling with large angle injection," J. Turbomach. **119**, 352–358 (1997).
[28]OpenCFD Ltd., 2019, "OpenFOAM v17.12," see https://www.openfoam.com/releases/openfoam-v1712/, 2017.
[29]F. Gori, M. Angelino, A. Boghi, and I. Petracci, "Preliminary numerical solutions of the evolution of free jets," in *Proceedings of ASME 2012 International Mechanical Engineering Congress and Exposition* (ASME Digital Collection, 2012), pp. 463–469.
[30]M. Angelino, A. Boghi, and F. Gori, "Numerical solution of three-dimensional rectangular submerged jets with the evidence of the undisturbed region of flow," Numer. Heat Transfer, Part A **70**, 815–830 (2016).
[31]K. Yamamoto, T. Murota, T. Okazaki, and M. Taniguchi, "Large eddy simulation of a pulverized coal jet flame ignited by a preheated gas flow," Proc. Combust. Inst. **33**, 1771–1778 (2011).
[32]M. Dianat, M. Skarysz, and A. Garmory, "A coupled level set and volume of fluid method for automotive exterior water management applications," Int. J. Multiphase Flow **91**, 19–38 (2017).
[33]F. Nicoud and F. Ducros, "Subgrid-scale stress modelling based on the square of the velocity gradient tensor," Flow, Turbul. Combust. **62**, 183–200 (1999).
[34]F. Duchaine, A. Corpron, L. Pons, V. Moureau, F. Nicoud, and T. Poinsot, "Development and assessment of a coupled strategy for conjugate heat transfer with large eddy simulation: Application to a cooled turbine blade," Int. J. Heat Fluid Flow **30**, 1129–1141 (2009).
[35]F. Duchaine, M. Boileau, Y. Sommerer, and T. Poinsot, "Large eddy simulation of flow and heat transfer around two square cylinders in a tandem arrangement," J. Heat Transfer **136**, 101702 (2014).
[36]S. Scholl, T. Verstraete, F. Duchaine, and L. Gicquel, "Conjugate heat transfer of a rib-roughened internal turbine blade cooling channel using large eddy simulation," Int. J. Heat Fluid Flow **61**, 650–664 (2016).
[37]S. Qin, M. Koochesfahani, and F. Jaberi, "Large eddy simulations of unsteady flows over a stationary airfoil," Comput. Fluids **161**, 155–170 (2018).
[38]A. Schindler, B. A. Younis, and B. Weigand, "Large-eddy simulations of turbulent flow through a heated square duct," Int. J. Therm. Sci. **135**, 302–318 (2019).
[39]T. M. Eidson, "Numerical simulation of the turbulent Rayleigh-Benard problem using subgrid modeling," J. Fluid Mech. **158**, 245–268 (1985).

[40]G. Grötzbach and M. Wörner, "Direct numerical and large eddy simulations in nuclear applications," Int. J. Heat Fluid Flow **20**, 222–240 (1999).
[41]X. Chen, Ph.D. thesis, Loughborough University, 2018.
[42]J. E. Mayhew, J. W. Baughn, and A. R. Byerley, "The effect of freestream turbulence on film cooling adiabatic effectiveness," Int. J. Heat Fluid Flow **24**, 669–679 (2003).
[43]A. Kohli and D. G. Bogard, "Effects of very high free-stream turbulence on the jet-mainstream interaction in a film cooling flow," J. Turbomach. **120**, 785–790 (1998).
[44]M. Klein, A. Sadiki, and J. Janicka, "A digital filter based generation of inflow data for spatially developing direct numerical or large eddy simulations," J. Comput. Phys. **186**, 652–665 (2003).
[45]M. C. Immer, "Time-resolved measurement and simulation of local scale turbulent urban flow," Ph.D. thesis (ETH Zurich, 2016).
[46]U. Piomelli and E. Balaras, "Wall-layer models for large-eddy simulations," Annu. Rev. Fluid Mech. **34**, 349 (2002).
[47]S. B. Pope, "Ten questions concerning the large-eddy simulation of turbulent flows," New J. Phys. **6**, 35 (2004).
[48]D. H. Leedom, Ph.D. thesis, Louisiana State University, 2009.
[49]A. Paszke, S. Gross, F. Massa, A. Lerer, J. Bradbury, G. Chanan, T. Killeen, Z. Lin, N. Gimelshein, L. Antiga, A. Desmaison, A. Kopf, E. Yang, Z. DeVito, M. Raison, A. Tejani, S. Chilamkurthy, B. Steiner, L. Fang, J. Bai, and S. Chintala, "PyTorch: An imperative style, high-performance deep learning library," in *Advances in Neural Information Processing Systems 32*, edited by H. Wallach, H. Larochelle, A. Beygelzimer, F. d'Alché-Buc, E. Fox, and R. Garnett (Curran Associates, Inc., 2019), pp. 8024–8035.
[50]S. B. Pope, "A more general effective-viscosity hypothesis," J. Fluid Mech. **72**, 331–340 (1975).
[51]J. X. Wang, J. L. Wu, and H. Xiao, "Physics-informed machine learning approach for reconstructing Reynolds stress modeling discrepancies based on DNS data," Phys. Rev. Fluids **2**, 034603 (2017).
[52]F. R. Menter, (2001). "Elements of inductrial heat tranfer predictions," in *16th Brazilian Congress of Mechanical Engineering (COBEM)*, Uberlandia, Brazil (2001).
[53]F. R. Menter, M. Kuntz, and R. Langtry, "Ten years of industrial experience with the SST turbulence model," in *Proceedings of the 4th International Symposium on Turbulence, Heat and Mass Transfer* (Begell House Inc., West Redding, 2003), pp. 625–632.
[54]J. Wu, H. Xiao, R. Sun, and Q. Wang, "Reynolds-averaged Navier-Stokes equations with explicit data-driven Reynolds stress closure can be ill-conditioned," J. Fluid Mech. **869**, 553–586 (2019).
[55]B. Basara and S. Jakirlic, "A new hybrid turbulence modelling strategy for industrial CFD," Int. J. Numer. Methods Fluids **42**, 89–116 (2003).
[56]M. L. A. Kaandorp and R. P. Dwight, "Data-driven modelling of the Reynolds stress tensor using random forests with invariance," Comput. Fluids **202**, 104497 (2020).
[57]P. Getreuer, "A survey of Gaussian convolution algorithms," Image Process. O Line **3**, 286–310 (2013).
[58]L. Andrei, A. Andreini, C. Bianchini, G. Caciolli, L. Mazzei, A. Picchi, and F. Turrini, "Effusion cooling plates for combustor liners: Experimental and numerical investigations on the effect of density ratio," Energy Procedia **45**, 1402–1411 (2014).